

Galactic cirri in deep optical imaging

Javier Román^{123*}, Ignacio Trujillo¹², and Mireia Montes⁴

¹ Instituto de Astrofísica de Canarias, c/ Vía Láctea s/n, E-38205, La Laguna, Tenerife, Spain

² Departamento de Astrofísica, Universidad de La Laguna, E-38206, La Laguna, Tenerife, Spain

³ Instituto de Astrofísica de Andalucía (CSIC), Glorieta de la Astronomía, 18008 Granada, Spain

⁴ School of Physics, University of New South Wales, Sydney, NSW 2052, Australia

July 3, 2019

ABSTRACT

The ubiquitous presence of Galactic cirri in deep optical images represents a major obstacle to study the low surface brightness features of extragalactic sources. To address this issue, we have explored the optical properties of cirri using g , r , i and z bands in the Sloan Digital Sky Survey (SDSS) Stripe82 region. Using state-of-the-art –custom made– image processing techniques, including the modeling and removal of the scattered light produced by the stars, we manage to isolate the optical diffuse emission by the cirri, allowing their photometric characterization. We find that their optical colors are driven by the dust column density: the cirri become redder as their $100\text{ }\mu\text{m}$ emission increases. This could explain the extended red emission previously found in dust clouds. In most cases, the optical colors of the Galactic cirri differ significantly from those of extragalactic sources. If future works confirm our findings, it would be possible the use of deep multi-band optical photometry (as the one produced by LSST) to identify the presence of cirri at a higher spatial resolution than those provided by far infrared observations. The combination of very deep data and multi-band photometry would make possible to build dust and extinction maps of unprecedented quality.

Key words. ISM: clouds – ISM: dust, extinction – Techniques: image processing – Techniques: photometric

1. Introduction

The current generation of deep optical surveys allows us, for the first time, to unravel critical issues of the hierarchical evolution of galaxies that are intrinsically connected with the low surface brightness Universe. For instance, the detection of galaxies of decreasing surface brightness (e.g. Sandage & Binggeli 1984; Impey et al. 1988; Dalcanton et al. 1997; Blanton et al. 2005; Mihos et al. 2015; Javanmardi et al. 2016; Mihos et al. 2018), the stellar halos and tidal features surrounding nearby galaxies (e.g. Bullock & Johnston 2005; Abadi et al. 2006; Johnston et al. 2008; Martínez-Delgado et al. 2010; Duc et al. 2015; Trujillo & Fliri 2016) or the intracluster light in galaxy clusters (e.g. Uson et al. 1991; Mihos et al. 2005; Rudick et al. 2010; Giallongo et al. 2014; Montes & Trujillo 2014, 2018) are all crucial observational pillars for testing the current Λ CDM cosmological paradigm (e.g. Moore et al. 1999; Klypin et al. 1999; Cooper et al. 2010, 2015).

The study of the faintest regions of the galaxies through the star counting technique reaches a depth equivalent to $30\text{ mag arcsec}^{-2}$ at detecting galaxy satellites (McConnachie 2012, and references therein) and $32\text{ mag arcsec}^{-2}$ at exploring galactic substructures as tidal features and stellar streams (e.g. Ibata et al. 2009; Tanaka et al. 2011; Ibata et al. 2014; Martin et al. 2014; McConnachie et al. 2018). However, the resolved star count method is only able to study the Local Universe, as it is limited by the spatial resolution of the images (e.g. 16 Mpc using the Hubble Space Telescope; Zackrisson et al. 2012), and stochasticity (Willman 2010). For this reason, integrated photometry studies are the only way to explore the low surface brightness components of galaxies beyond the Local Group. However, the

use of integrated photometry is affected by systematic effects, severely restricting the surface brightness limits of the optical data. In particular, we can number the following: i) poor data reduction processes that can create artificial gradients and different artifacts in the images, ii) incorrect subtraction of the sky background that removes or over-subtracts the low surface brightness information around extended sources and iii) scattered light contamination from sources due to the extended point spread function (PSF) and internal reflections present in the images. Different approaches have been tried to minimize these effects, such as better astronomical data reduction pipelines (Akhlaghi & Ichikawa 2015; Borlaff et al. 2019), improvements in the observational techniques (e.g. Ferrarese et al. 2012; Duc et al. 2015; Trujillo & Fliri 2016), a better characterization of the PSF and internal reflections due to optical instrumentation (Slater et al. 2009; Sandin 2014; Infante-Sainz et al. 2019 in prep.) or the development of simple optic telescopes (Abraham & van Dokkum 2014; Muslimov et al. 2017; Valls-Gabaud & MESSIER Collaboration 2017).

Despite all the observational and technical advances aiming to improve the quality of deep optical datasets, the presence of interstellar material from our own Galaxy reflecting the starlight (Elvey & Roach 1937; Henyey & Greenstein 1941; Sandage 1976; Mattila 1979) in unavoidable, harming the study of the faintest regions of galaxies. These filamentary clouds of dust, called "Galactic cirri", have their peak emission in the far infrared due to their low temperature (Low et al. 1984; Veneziani et al. 2010). However, Galactic cirri are detectable in optical (de Vries & Le Poole 1985; Laureijs et al. 1987; Witt et al. 2008) and ultraviolet (Witt et al. 1997; Boissier et al. 2015) wavelengths, being reflective in those spectral ranges. With the increasing depth of optical observations, the presence of cirri has become a

* e-mail: jromanastro@gmail.com

major obstacle in the study of faint extragalactic features even at high Galactic latitudes, mimicking their shape and brightness, creating confusion (e.g. Chiboucas et al. 2009; Cortese et al. 2010; Sollima et al. 2010; Rudick et al. 2010; Davies et al. 2010; Chiboucas et al. 2013; Hodges-Kluck & Bregman 2014; Besla et al. 2016; Duc et al. 2018; Barrena et al. 2018; Ramírez-Moreta et al. 2018). Far infrared or sub-millimetre full-sky maps, as the IR Astronomical Satellite (IRAS) mission or the Planck Space Observatory, are used to identify the presence of cirri in the optical images. However, the poor spatial resolution of the far-infrared and sub-millimetre images produced by these instruments ($\text{FWHM} \approx 5$ arcmins; Miville-Deschénes & Lagache 2005; Lamarre et al. 2003) makes them inefficient for the study of small angular scale features. Only with the availability of better spatial resolution far infrared data, as the ESA Herschel Space Observatory (FWHM of 18 arcseconds in the $250\ \mu\text{m}$ band; Pilbratt et al. 2010) it is possible to identify correctly, or even remove, the dust foreground contamination (see Mihos et al. 2017). Unfortunately, the Herschel Space Observatory data only covers a modest portion of the sky. Therefore, it would be desirable to use the optical data itself to identify the presence of cirri without the need to resort to complementary data at other wavelengths. This means, ultimately, to define accurately the range in optical colors of the Galactic cirri, allowing to discern between them and extragalactic sources, if possible.

Previous studies of the optical properties of the Galactic cirri (e.g. Guhathakurta & Tyson 1989; Witt et al. 2008; Ienaka et al. 2013) have neglected important systematic effects, as the presence of scattered light by bright stars due to the PSF. This effect, for instance, could have a significant impact on the photometry of the cirri due to their extremely low surface brightness, especially in areas where the dust clouds have a low column density or surface brightness.

The imminent arrival of the Large Synoptic Survey Telescope (LSST; LSST Science Collaboration et al. 2009) and the new generation of extremely large telescopes, will light up the presence of Galactic cirri at any Galactic latitude. It is, therefore, a priority for the extragalactic community to address the problem of the cirri contamination in order to study the low surface brightness Universe. This issue is also crucial in other matters as the characterization of the Cosmic Microwave Background and its polarization (e.g. Planck Collaboration et al. 2011; Das et al. 2014) or the Infrared Cosmic Background (e.g. Thacker et al. 2013). In this work, we aim to carry out a comprehensive photometric analysis of the Galactic cirri, taking into account the possible systematic uncertainties derived from the extremely low surface brightness regime. The goal is to provide the colors of the cirri in optical wavelengths.

This paper is structured as follows: In Section 2 we describe the data and its processing. The correlation between the far IR and optical bands is explored in Section 3. In Section 4, we describe the optical colors of the Galactic cirri. We address our main conclusions in Section 5. We use the AB photometric system throughout this work.

2. Data and data processing

A common problem affecting deep optical surveys is the over-subtraction of flux around extended sources. This is the result of aggressive sky subtraction (see a full discussion and a way to deal with this problem in Borlaff et al. 2019, using the Hubble Ultra-Deep Field dataset). Public versions of the Hyper Suprime-Cam Subaru Strategic Program (HSC-SSP) (Aihara et al. 2018) or the Dark Energy Camera Legacy Survey (DECaLS) (Dark En-

ergy Survey Collaboration et al. 2016) are severely affected by an aggressive sky subtraction. This circumstance prevents the study of extended diffuse emission, which misidentified as the sky itself, it would be systematically subtracted. To overcome this problem, in this work we use data from the IAC Stripe82 Legacy Survey (Fliri & Trujillo 2016). This dataset consists in a new reduction of the SDSS Stripe82 data (Abazajian et al. 2009) with the aim of preserving the faintest extended features, minimizing the over-subtraction around sources. The Stripe82 region covers a 2.5 degree wide stripe along the Celestial Equator in the Southern Galactic Cap ($-50^\circ < \text{R.A.} < 60^\circ$, $-1.25^\circ < \text{Dec.} < 1.25^\circ$) reaching a total of 275 square degrees. The total exposure time per field is around 1 hour, using the 2.5m Telescope at Apache Point Observatory (SDSS) in all the five SDSS filters (u, g, r, i, z). The pixel scale is 0.396 arcsec and the average seeing is around 1 arcsec. In this work, we use the new set of rectified images of the survey described by Román & Trujillo (2018) in which the residuals of the co-adding process have been removed. This produces high-quality and homogenized deep images, allowing a clean photometry of the faintest structures. The average surface brightness limits of the dataset are μ_{lim} (3σ ; $10'' \times 10''$) = $28.0, 29.1, 28.6, 28.2$ and 26.6 mag arcsec $^{-2}$ for the u, g, r, i and z bands respectively. We describe in detail how these limits are calculated in Appendix A.

Although the IAC Stripe82 dataset preserves the diffuse emission, the photometry of extended sources is not straight forward to obtain. For instance, the scattered light produced by the PSF wings of the stars strongly contaminates the faint cirri emission. Additionally, an exquisite masking of sources is necessary to obtain a reliable photometry of the cirri. In the following, we describe the data processing performed in order to isolate the Galactic cirri flux.

2.1. Modeling the scattered light produced by the stars

The removal of the scattered light produced by the stars is becoming a common technique to obtain clean photometry of extremely low surface brightness sources. For instance, Slater et al. (2009) modeled the internal reflections produced by the stars with the Burrell Schmidt telescope (Rudick et al. 2010; Watkins et al. 2014, 2015, 2016, 2017; Mihos et al. 2017; Watkins et al. 2018), Trujillo & Fliri (2016) modeled the scattered light by stars in very deep observations of the UGC 00180 galaxy using a PSF characterization of the 10.4m GTC telescope and Karabal et al. (2017) modeled the internal reflections and PSF using images of the Canada France Hawaii Telescope (CFHT) to provide reliable deep photometry of galaxies.

The specific characteristics of the internal reflections due to the optical instrumentation of the telescope is an important issue to take into account when modeling the stars. Depending on the extension of the reflections, the sum of all of them can contaminate a significant fraction of the total area of the image. This circumstance would require a modeling of the reflections. In the specific case of the IAC Stripe82 Legacy Survey, the internal reflections are located at the same spatial position in each single exposure, and therefore, in the final coadd. Additionally, these reflections only subtend a small angular size (up to $30''$, see Infante-Sainz et al. 2019 in prep.), being relatively faint and, only noticeable for bright stars. Consequently, we consider not necessary to model these reflections, but only the PSF (image of a point source through the main optical path, without reflections on the CCD). The sum of the scattered light by all the stars in a given field due to the PSF is what we call the "scattered light field".

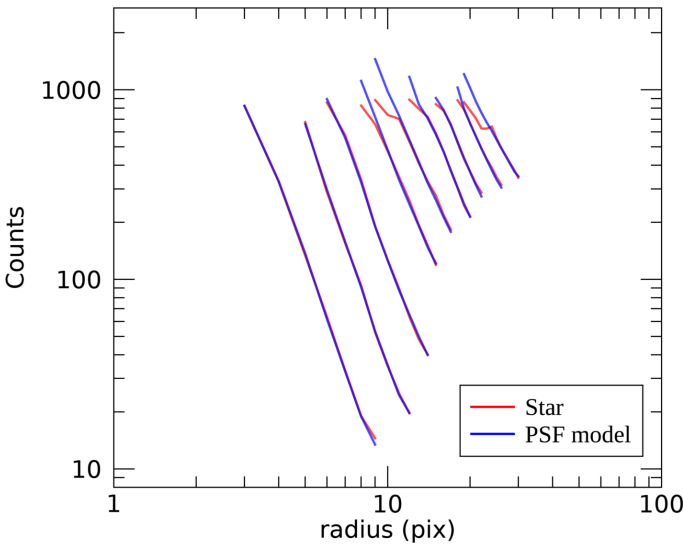


Fig. 1. Surface brightness profiles in the g band of real stars together with the fitted PSF models in a random field of the Stripe82 region. The plot shows the profiles of the fitted stars (red) and the profile of the flux scaled PSF models (blue). Nine stars are fitted in this example, with magnitudes ranging approximately between 7.5 and 15.5 in the g band. The profiles cover the radial region used to calculate the flux of each star. The radial region selected for the profile fitting is dynamic for each star and depends on the circumstances of saturation, crowding or magnitude of the star (see main text). Note that the saturation region appears above approximately 800 counts, creating severe deviations from the PSF model in the inner region of the profiles of the brightest stars due to CCD bleeding.

Obtaining the scattered light field means characterizing accurately the PSF. Once the PSF model is obtained, the scattered light field is defined by the position and fluxes of the stars in the image. Thus, the only information needed to produce the scattered light field is the PSF and the coordinates and fluxes of the stars to be modeled. In Appendix B we describe the process followed to model the PSF for the IAC Stripe82 Legacy Survey in the five SDSS bands.

To obtain the exact coordinates and fluxes of the stars, there is a number of practical problems, as the inner saturated region of the bright stars or the presence of adjacent or overlapping sources. These difficulties make the process of fitting the stars not straightforward. In this work, we have created a specific pipeline that obtains precise positions and accurate photometry of the stars, even if the stars are saturated. The main tasks of this pipeline are summarized on what follows.

For each field we produced a catalog of stars. We runned SExtractor (Bertin & Arnouts 1996) obtaining the position and stellarity for each source in the field. We classify as stars those sources with stellarity (CLASS_STAR) higher than 0.75 in the r -deep band, a deep $g + r + i$ combined image provided by the IAC Stripe82 survey. This criterion filters the stars by exclusively selecting PSF-like sources. However, very bright stars do not match this criterion, as they are detected with a lower stellarity due to strong inner saturation and bleeding. Since these stars are very bright, and hence very few, we included their coordinates manually, hence completing the final catalog.

The next step is to obtain accurate spatial coordinates of the selected stars, which is crucial for the PSF modeling (Lu et al. 2018). For each star, we masked the saturation region (if present) by masking pixels with counts above the saturation threshold for each band. We also masked all the sources that are adjacent or

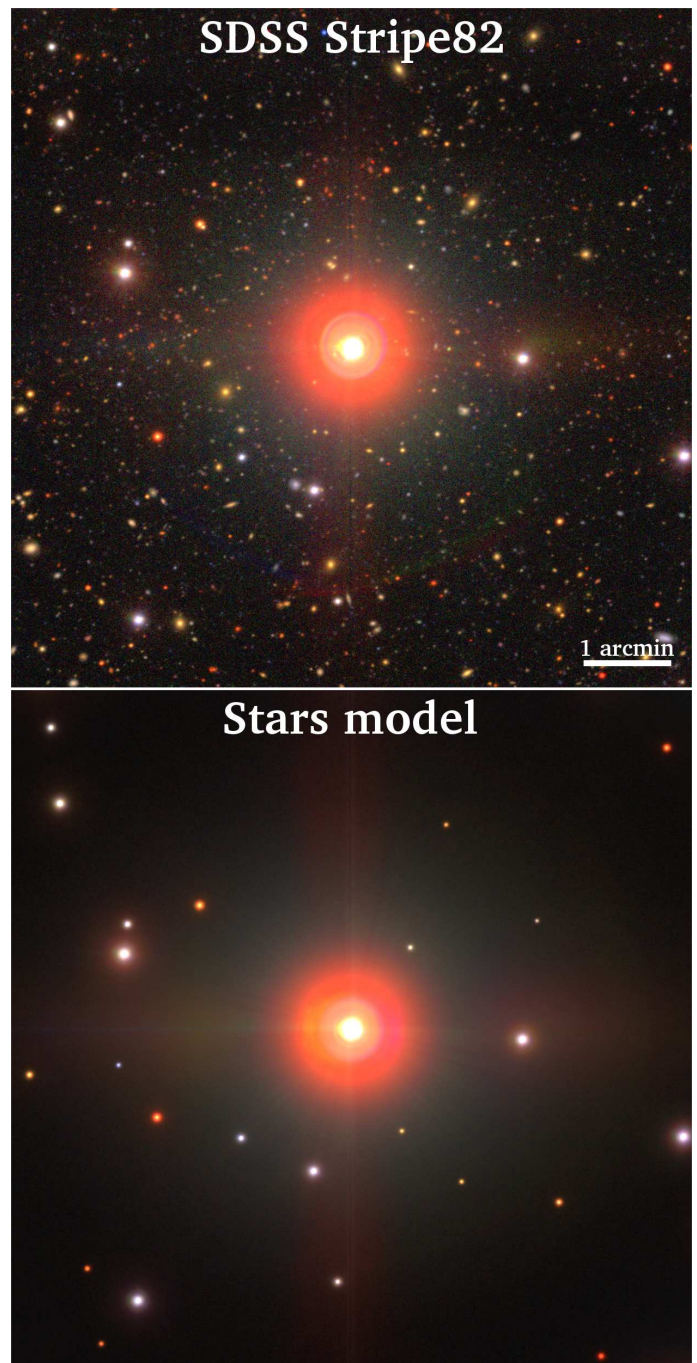


Fig. 2. Color composite image of a real bright star and its surrounding field in the Stripe82 region using g , r and i SDSS bands (upper panel). In the bottom panel we show a model of the bright and other fainter stars of the same field.

overlapping the stars using the segmentation maps provided by SExtractor. Because these detection maps do not cover well enough the sources, in particular the faint external regions, we expanded the masks to cover most of the flux of the sources. To obtain accurate spatial coordinates for each star, we fitted a Moffat function to the masked star using the IMFIT (Erwin 2015) package and we got the coordinates of the centre provided by this fitting.

Once the star is masked and centered, we performed the flux fitting. We fitted the radial profile of the PSF model to the profile of the star. We adopted this methodology as the profiles are more

resistant to masking residuals, crowding or any artifact that could remain in the images. For each star, we selected a range in radius for the profile fitting. This range is dynamic and depends on the tentative magnitude provided by SExtractor (imprecise due to saturation among other factors) and the crowding of adjacent sources to the star. In general terms, the higher the luminosity of the star, the larger the range in radius, and if the star has an adjacent source, this range will be truncated to the point where the profile increases with the radius. With this procedure, we select a range in the profile with a high signal to noise, which depends on the luminosity of the star, avoiding reaching areas where adjacent sources could deviate the flux measurement. Once the profile of the star is obtained, we scaled it to match the normalized PSF profile, giving the flux of the star. To obtain the most accurate measurement possible, we averaged the flux ratios between the star and the PSF profiles at each radius, discarding outlier values beyond 2σ . This provides a robust flux value for the star. Fig. 1 shows an illustrative example of how accurate the profiles of the stars are fitted using this methodology.

Repeating this entire process for the complete catalogue of stars, we obtained the positions and integrated fluxes of all the stars in the field. For the purposes of this work, we modeled all the stars up to magnitude 15 in the r-band for reasons of computational efficiency. We have found that for a typical Stripe82 field, the scattered light field produced by stars fainter than 15 magnitude is negligible.

Finally, using the software SWARP (Bertin et al. 2002), we created the scattered light field by placing PSF models with the calculated positions and fluxes of the stars over a blank field. We show in Fig. 2 an example of an arbitrary field modeled with our procedure. The average number of fitted stars is approximately 400 per square degree. Due to the strong presence of artifacts, i.e., "ghosts", in the u band, and the high sky background fluctuations in this band, we restrict ourselves to the more reliable g, r, i and z bands for further analysis.

2.2. Properties of the scattered light field produced by stars

Obtaining the scattered light field model provides interesting information about its effect on the data. The availability of the g, r, i and z SDSS bands gives us the possibility to obtain a photometric description of the colors of the scattered light produced by the stars. In Fig. 3, we show a random field of 1×1 degree of the IAC Stripe82 Legacy Survey. In the upper left panel, we present the surface brightness map produced by the stars in the r band. In the lower plot of that panel, we show the surface brightness distributions of all the pixels in the image for the g, r, i and z bands. As can be seen, the surface brightness distributions of the scattered light field vary between different bands. In the case of the r band, there is an average surface brightness of approximately $29 \text{ mag arcsec}^{-2}$, similar to the value reported by Trujillo & Fliri (2016) using the GTC telescope in that same band (see also work by Slater et al. 2009). The average surface brightness of the scattered light field increases as the band gets redder, ranging from a typical surface brightness of $30 \text{ mag arcsec}^{-2}$ in the g band to $28 \text{ mag arcsec}^{-2}$ in the z band. It is of course, expected, as the average star is brighter in redder optical bands. Another way to look at this is shown in the other panels of Fig. 3, where the color maps of the scattered light field are shown, together with their color distributions, having mean red colors. However, the colors of the scattered light are far from having an homogeneous distribution in the image, suffering from strong color variations at small spatial scales. This effect is particularly striking in those colors containing the i band. The reason is the complex

Table 1. Summary of SExtractor configuration parameters applied for the different masking layers. The enlarged mask size is given in pixels units (0.396 arcsec).

Mask	DETECT MINAREA	DETECT MAXAREA	DETECT THRESH	BACK SIZE	Enlarged mask size
1	5	150	3	10	0
2	150	500	3	10	5
3	450	1500	2	10	15
4	1900	7500	4	200	20
5	1000	2500	3	10	30
6	7000	inf.	4	100	30

PSF far-wing could affect color severely! (van Dokkum 2010)

PSF structure in this band, with a bump within 30 arcsec from the center (de Jong 2008; Infante-Sainz et al. 2019 in prep., see also Fig. B.2). This produces complex color patches around the stars, clearly noticeable in the brightest star in Fig. 2.

Although the vast majority of the scattered light field in an image has low surface brightness, it can have a significant impact on the photometry of extremely faint sources, as in the case of Galactic cirri. In fact, the average surface brightness of the Galactic cirri analyzed in this work is well below $26 \text{ mag arcsec}^{-2}$ in the r band. Therefore the scattered light field could strongly affect the global photometry of the cirri. Note that the results shown in this section are only descriptive of the data used in this work; SDSS data from the IAC Stripe82 Legacy Survey. The use of another dataset with different PSFs could create different scattered light fields and derived photometric properties.

2.3. Isolating the extended diffuse emission of the Galactic cirri

The modeling and subtraction of the stars produces images almost free of contamination by scattered light. However, faint stars, galaxies, residuals of the scattered light subtraction and different artifacts still remain in the image (see Fig. 4). In order to isolate the diffuse emission of the Galactic cirri in the images, it is necessary to mask accurately all the sources. However, the masking of low surface brightness structures is not an easy task. For example, SExtractor is not able to detect the faintest outer regions of the sources, producing an incomplete masking and a potential source of contamination. After testing several options, we ended up with a modified masking process based on SExtractor. The reason is that SExtractor detects sources targeting exclusively stars and galaxies, being inefficient in the detection of amorphous structures, as in the case of cirri. In this sense, the ineffectiveness of SExtractor in the detection of complex low surface brightness features works to our advantage, since only stars and galaxies are aimed to be masked. To mask completely the sources, we constructed a specific algorithm to improve the masks provided by SExtractor. It consists of six different layers of masking, focused in the detection of different sizes and deblending levels (sources over sources), each one with a different enlargement of the mask. In Table 1, we list the SExtractor parameters for each masking layer. This masking sequence manages to cover all the sources, exposing only the diffuse emission by the cirri in the images. This masking is constructed in a conservative way, meaning that the masks are systematically larger than the actual size of the sources. However, due to the large area occupied by the cirri in relation to the sources to be masked, that loss of area is acceptable for the purposes of this work. Since our goal is precision photometric measurements of Galactic cirri, any possible systematic uncertainty should be treated conservatively.

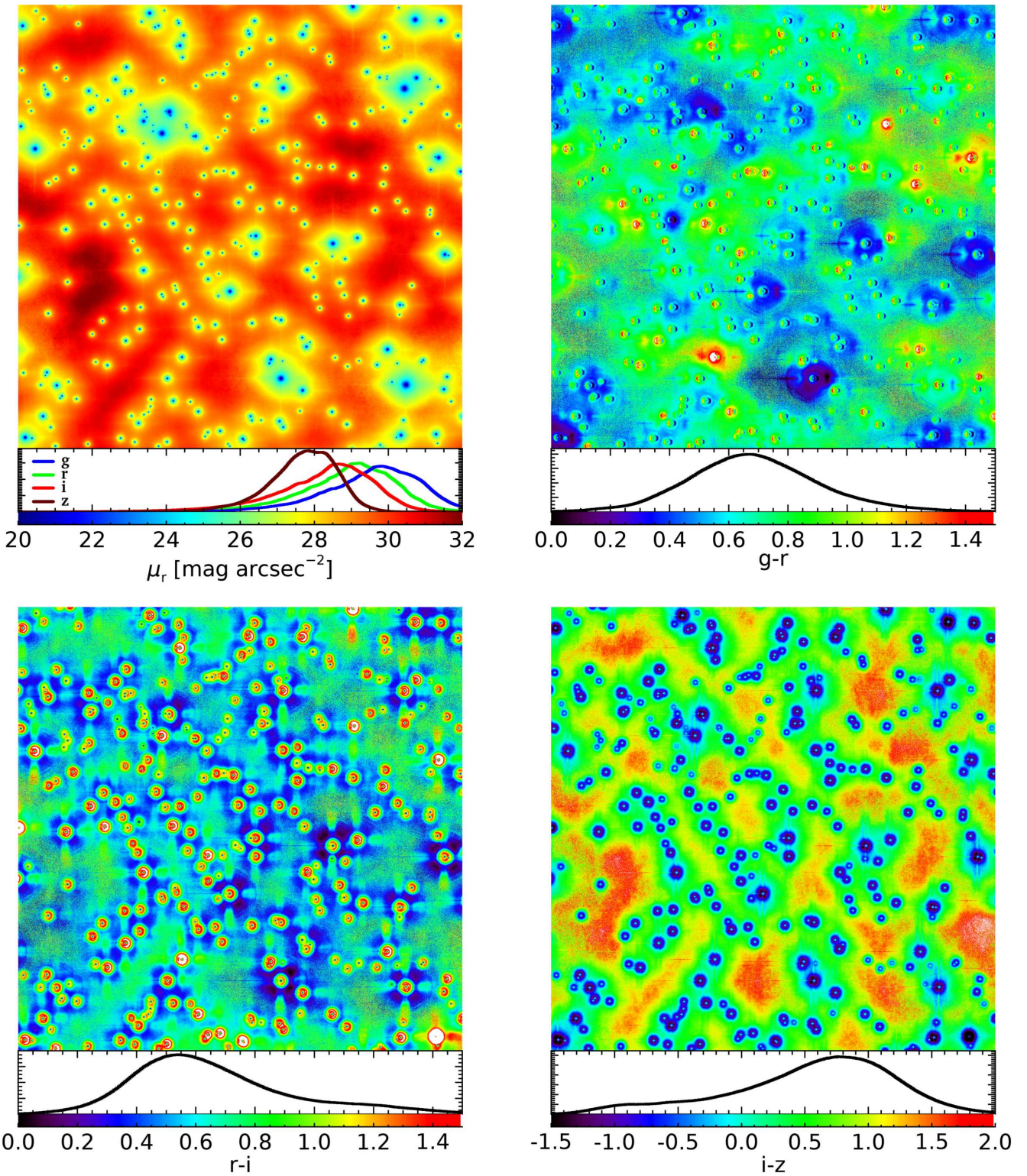


Fig. 3. Photometric properties of the scattered light field produced by the stars on a random field of 1×1 degree of the IAC Stripe82 Legacy Survey. The upper left panel shows the surface brightness distribution of the pixels of the field in the r band. The upper right, bottom left and bottom right panels show the $g-r$, $r-i$ and $i-z$ colors respectively. The bottom plots in each panel represent the distribution histograms.

The masking algorithm has as input the original r -deep band image of the field, with all the stars present in the image. All the masks obtained from the different steps of the algorithm described above are combined in a unique mask, which is applied to all the images in the different bands corrected from the scattered light field. Note that the presence of stars in the input im-

age facilitates the masking of the centers of the removed stars (only the centers, since SExtractor is not able to mask the PSF wings of the stars), covering all the subtraction residuals. The application of this masking process produces an excellent isolation of the diffuse emission by cirri. However, "ghosts" and different artifacts still remain in the images. Nevertheless, these

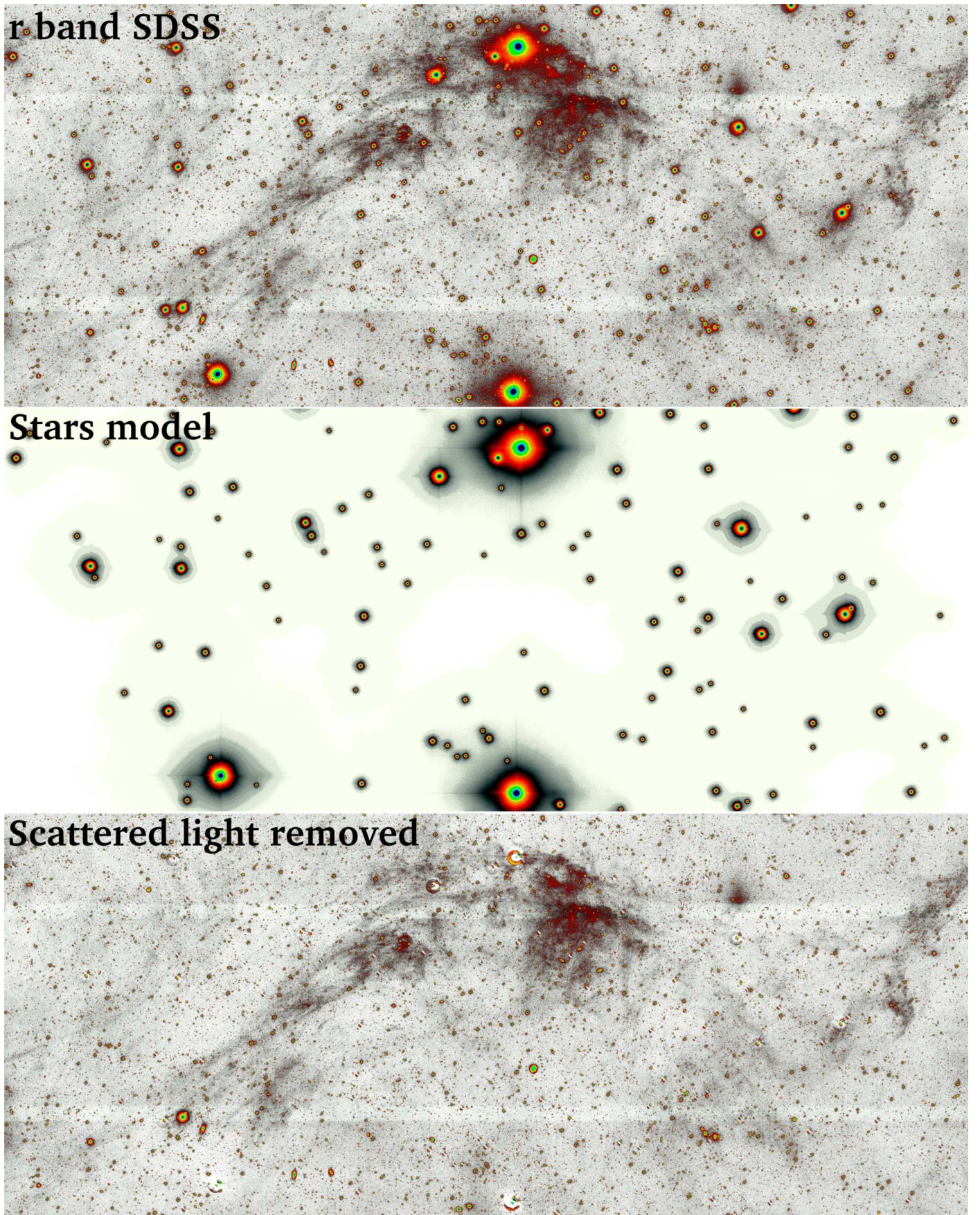


Fig. 4. Example of the process of removing the scattered light produced by the stars in Stripe82 images. Top panel: Original IAC Stripe82 field in the r-band. Middle panel: Model of the scattered light field produced by the stars. Bottom panel: Same as the top panel but with the scattered light field subtracted. The pixel scale is 0.396 arcseconds.

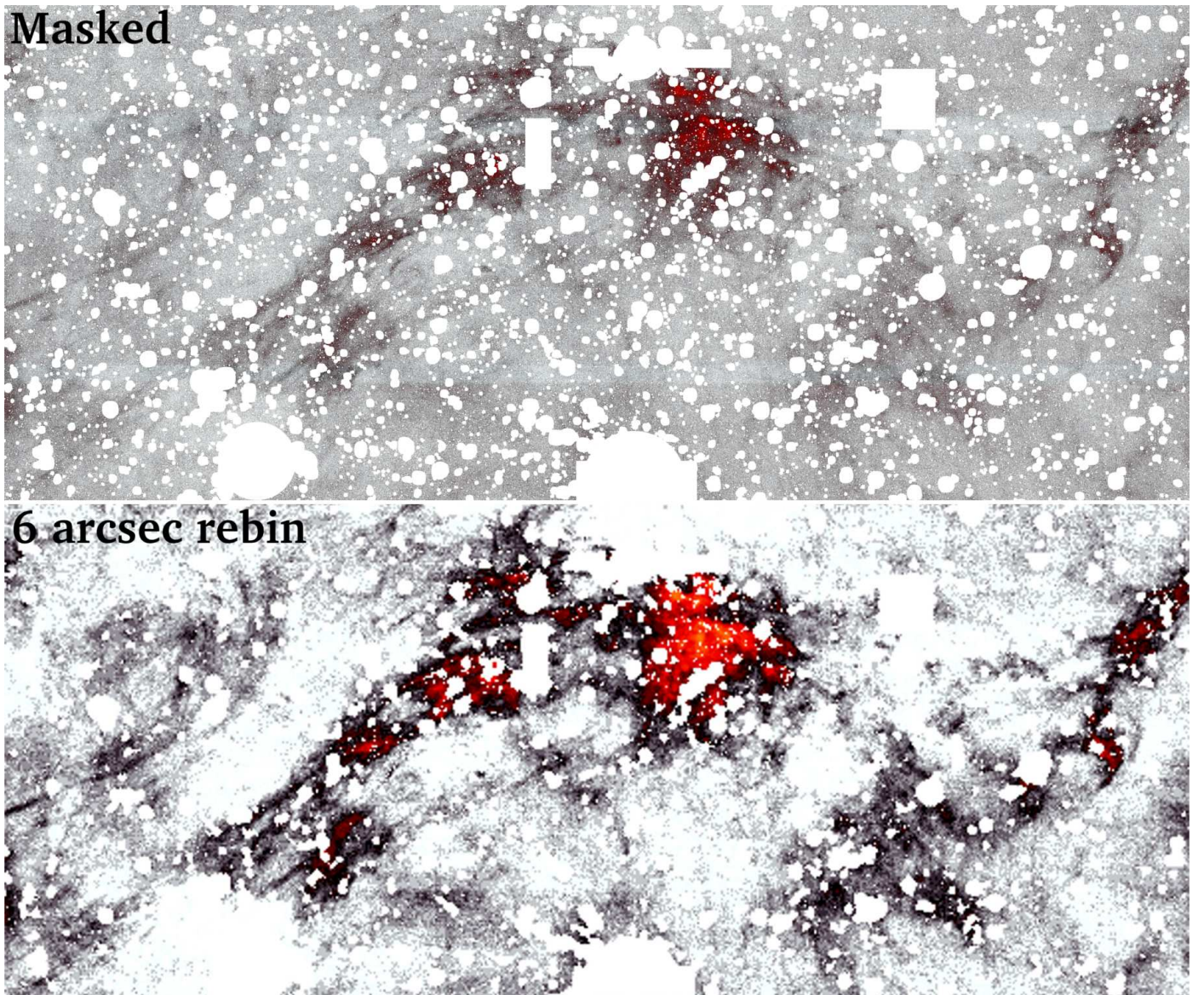


Fig. 5. The same example as in Fig. 4 showing the masking process (upper panel) and rebinning (bottom panel). The images are scattered light field removed. Masked regions appear as white color.

are well documented¹ and are easily identified visually in single band images or through color maps, presenting extreme colors against real sources. Therefore, we applied an additional manual masking focused on those artifacts. We show an illustrative example of the final result of the entire masking process in Fig. 5.

As a final step, we increase the pixel size of the images to enhance the signal to noise ratio of the final image. Due to the large angular size of the Galactic cirri, there is a large margin to increase the pixel size without a reasonable loss of spatial resolution. The increase of the pixel size enhances the signal to noise by reducing the Poisson noise as the result of averaging the original pixels into a larger one. We choose a 6 arcsec final pixel scale as a compromise between optimal spatial resolution and the depth of the images. With this pixel size the average surface brightness limits in pixel to pixel variations are $\mu_{lim}(3\sigma; 6'' \times 6'') = 28.5, 28.0, 27.6$ and 26.0 mag arcsec $^{-2}$ for the g, r, i and z bands respectively (see Appendix A).

$= 28.5, 28.0, 27.6$ and 26.0 mag arcsec $^{-2}$ for the g, r, i and z bands respectively (see Appendix A).

After the rebinning process we found a small fraction of pixels (less than 1 percent) whose values are much higher than adjacent pixels. These pixels appear prominent in comparison with the soft background light of the diffuse emission. By inspecting the images, we detected that these hot pixels are the result of residuals in the masking process using the original pixel scale. These are typically faint tidal features or haloes of galaxies, not detectable in the processed image but enhanced in the rebinned images. To remove these residuals, we carried out a last masking step in the rebinned images. Due to the isolated nature of these hot pixels in comparison with the smooth background of the diffuse emission, we masked pixels with counts 5σ above the noise with respect to the average value of their adjacent pixels. With this, we guarantee that the masked pixels are not statistical fluctuations of the Poisson noise but true anomalous fluxes coming from residuals in the masking process.

Finally, we calibrated the reference sky background level. To do this we performed a masking of the diffuse light present in the

¹ <http://skyserver.sdss.org/dr12/en/tools/places/page6.aspx>

images through a strong gaussian smoothing with a kernel width of 30 arcsec to the 6 arcsec pixel scaled masked images and we ran SExtractor with a specific setup to detect most of the diffuse emission. This detection of the diffuse light in the images based on SExtractor is not accurate, therefore not reliable for photometric measurements, but it is sufficient to hide most of the diffuse emission, leaving unmasked the regions that can be considered as a sky background. We used an algorithm of the type mean-median, specifically designed to obtain a reliable sky background level even in very contaminated fields, to compute the reference flux sky level. We used the routine SKY from IDL to perform this task.

3. Galactic cirri: Optical vs. far IR counterparts

The data processing described in the previous section allows us to isolate the extended diffuse emission present in the optical data. However, it is necessary to discern whether this diffuse emission is due entirely to Galactic dust, or on the contrary, there is another source of diffuse emission in the optical, including residuals of the data processing. Since Galactic cirri appear clearly at far IR wavelengths, any emission by cirri in the optical should have an infrared counterpart, and equivalently, any optical diffuse emission without IR counterpart could be considered not due to cirri.

To do that, we performed a direct photometric comparison of the diffuse emission present in the optical data of the IAC Stripe82 Legacy Survey with the diffuse emission found in the far IR in the Herschel Multi-tiered Extragalactic Survey (HerMES; Levenson et al. 2010; Viero et al. 2013) and the Hershel Stripe82 survey (HerS; Viero et al. 2014). These data cover a wide region matching the Stripe82 area within $350^\circ < \text{R.A.} < 36^\circ$ using the Spectral and Photometric Imaging Receiver (SPIRE) of the *Herschel Space Observatory* at 250, 350, and 500 μm bands. We used the HerS-HeLMS-XMM-LSS combined SPIRE maps (DR4) publicly available on the Herschel Database in Marseille². Though this far IR survey is focused on the study of extragalactic sources as infrared-emitting dusty star-forming galaxies or active galactic nuclei, Galactic cirri are detectable in the area mapped by the survey. The relative high spatial resolution of this far IR data compared, for instance, with the IRAS survey, allows a direct photometric comparison of the extended diffuse emission with the optical bands. For the purposes of this work, we used only the 250 μm band due to its higher angular resolution (6" pixel scale, 18.1" FWHM) and optimal wavelength for the detection of the Galactic dust emission.

In Fig. 6 we show the HerS-HeLMS-XMM-LSS map at 250 μm and the footprint of the SDSS Stripe82 survey indicated by horizontal blue lines. While the mapped area has a relatively low presence of dust, some conspicuous filamentary clouds are clearly visible in the 250 μm image. We selected an area of 3×2 degrees with the highest presence of Galactic cirri, labelled in Fig. 6 as "Cirrus field". We did not conduct any analysis of additional regions due to the low emissivity of the clouds present in the footprint, both in the far IR and in optical bands, especially in the shallower z band. We also selected an area free of Galactic cirri, with a size of 1.0×1.5 degrees, being considered as a control field, labelled in Fig. 6 as "Control field". For the two selected fields, we created five mosaics, one for each of the 250 μm , g , r , i and z bands. The images in different bands were matched astrometrically allowing a pixel to pixel comparison. We performed the data processing described in Sec. 2 for the

optical bands. Additionally, we performed a masking of the 250 μm image, focused on extragalactic sources leaving unmasked the emission by Galactic cirri. Finally, because the FWHM of the 250 μm band is 18 arcseconds, we performed a 3-pixel kernel smoothing to the optical images (pixel scale of 6 arcseconds), ensuring that the optical bands match the resolution of the 250 μm data.

We plot the correlation between the 250 μm and optical bands in the lower panel of Fig. 6 for the Control field (upper row) and for the Cirrus field (lower row). Each pixel of the image is a dot in the plot. The detection limits for each band are indicated as dashed lines in red, orange and green, corresponding to the 1σ , 2σ and 3σ depth limits, respectively. We used the values of the 250 μm depth detection limit provided by Viero et al. (2014) corresponding to $1\sigma = 13 \text{ mJy beam}^{-1}$. The analysis in the Control Field shows a distribution compatible with Poisson noise in both 250 μm and optical bands, being the fluctuations of such noise consistent with the detection limits of each band. We find no evidence of optical diffuse emission in the Control field by visual inspection of the images, neither in the correlation plot between the optical and far IR bands, existing only random fluctuations in the sky background due to the drift scan mode of the optical observations, and all of them below the detection limits. Conversely, we find in the Cirrus field a tight correlation between all the optical bands and the far IR emission. While for the g , r and i bands there is a sufficient margin to observe this correlation in a wide range of surface brightness above the detection limits (around $2.5 - 3 \text{ mag arcsec}^{-2}$), in the z band the magnitude range of detection is significantly smaller due to the shallower depth of this band. Nevertheless, it is still possible to observe such correlation above the 3σ limit in areas with surface brightness above $26 \text{ mag arcsec}^{-2}$ in the z band. It is worth noticing that the depth of the Stripe82 survey is such that the signal to noise of the cirri in the optical images is higher than in the far IR. This can be seen by observing that the cirrus emission is a factor of ~ 2 further away from the 3σ detection limit in the optical bands (except for the z band) than for the 250 μm band. It is also remarkable the similar emission in surface brightness of the r , i and z bands, at least in the brightest regions, being the emission in the g band $\sim 0.5 \text{ mag arcsec}^{-2}$ fainter. This would correspond to $r-i$ and $i-z$ colors close to 0 mag, while the $g-r$ color would be considerably redder. We will explore this matter in detail in the next section.

We show in Fig. 7 a visual comparison of the Cirrus field in the far IR 250 μm band with the processed optical r band. The morphology of the diffuse emission in both images is remarkably similar, existing an optical counterpart to what is detected in the far IR. As can be noted, the presence of sky background fluctuations and oversubtraction due to the observational drift scan mode are the main limitations in the recovery of the diffuse emission in the optical dataset. However, these artifacts are below the detection limits. The present analysis is compatible with the idea that the far IR emission by Galactic cirri has a counterpart in the optical. It is worth also emphasizing the extremely low surface brightness of the features detected in this analysis.

The Herschel data allow to explore the optical counterparts of Galactic dust clouds with a relatively high resolution (FWHM = 18 arcseconds). However, the scarce presence of Galactic cirri in the footprint of the HerS-HeLMS-XMM-LSS maps makes the conclusions obtained so far limited to a particular region, both in Galactic latitude and in IR emission. In order to obtain a more significant sample, we have expanded our analysis to other areas within the Stripe82 region with presence of Galactic cirri. Even though the resolution of available full-sky surveys as the IRAS 100 μm band (FWHM = 5 arcmin) is significantly worse than

² <https://hedam.lam.fr/HerMES/>.

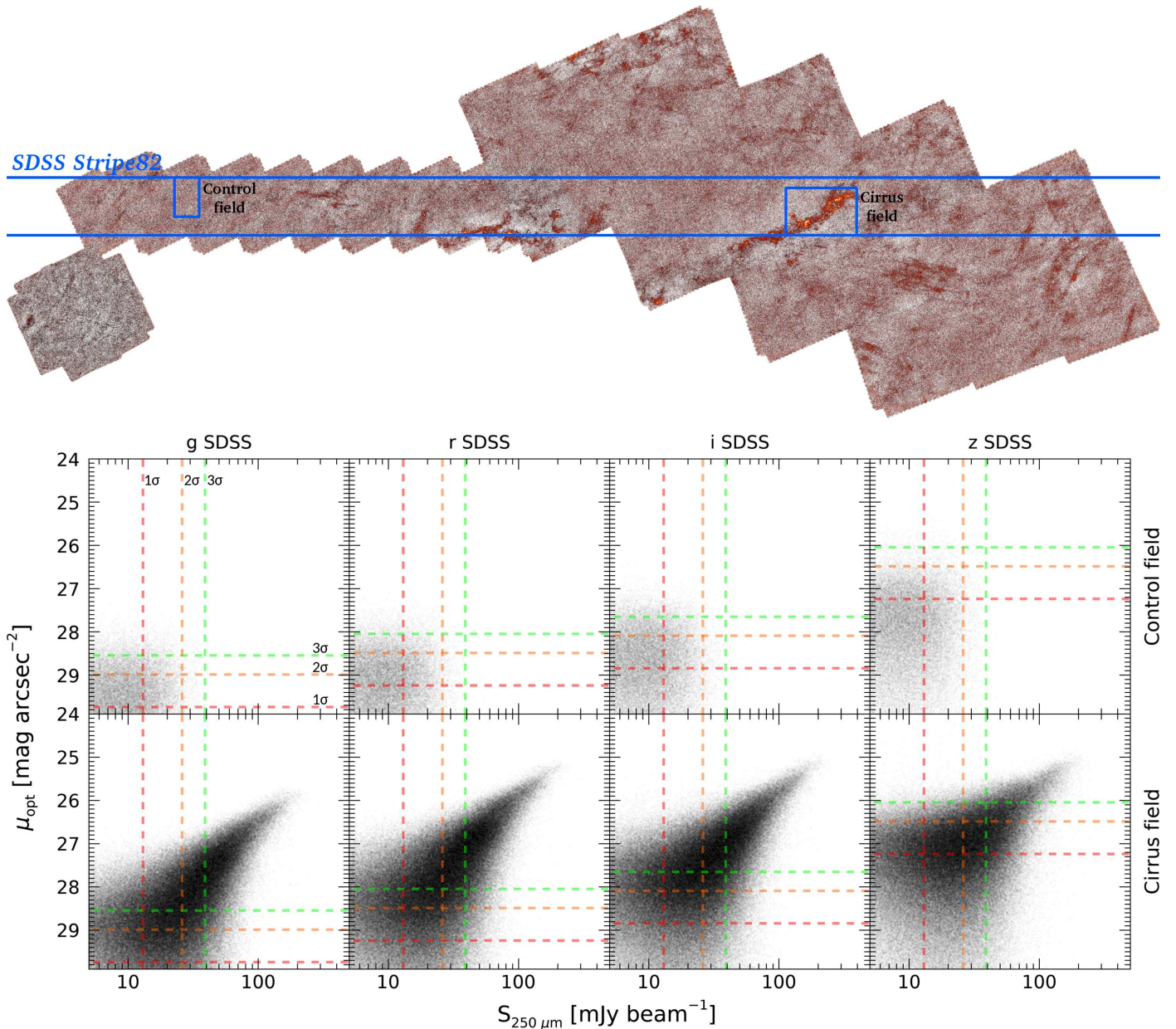


Fig. 6. Optical vs. far IR diffuse emission. In the upper panel is shown the Herschel Stripe82 survey footprint overlaid with the SDSS Stripe82 footprint. The lower panels show the correlation between the diffuse emission in the far IR data and g , r , i and z optical bands for the Control field (upper row) and the Cirrus field (lower row). The dashed red, orange and green lines correspond to the 1σ , 2σ and 3σ detection limits in each band, respectively.

that of the Herschel SPIRE data, it can still be used to check for the presence of Galactic cirri in the explored areas. We visually compared a set of fields where the data processing in Sec. 2 has been carried out. The description of the fields and the criteria for selecting them can be found in the next section. We found a good match between the optical data and its far IR counterpart within the resolution limits of IRAS, and more importantly, no obvious optical diffuse emission is detected without a far IR counterpart. We show in Fig. 8 an example field of Galactic cirri emission and its counterpart in the $100\text{ }\mu\text{m}$ IRAS band. This comparison shows something remarkable: the great advantage of deep optical imaging in revealing the morphology of the Galactic dust clouds in a more effective way than the IRAS maps. While the far IR has traditionally been used to detect the presence of interstellar dust, our analysis shows that it is possible to obtain a map of Galactic dust with higher spatial resolution and greater depth

using optical data. In summary, the analysis carried out in this section shows that:

1. The scattered light field removal process and subsequent masking of the optical images is highly effective in isolating the optical diffuse emission. The IAC Stripe82 Survey ultimate limitation are the sky background fluctuations. Nonetheless, these are below the surface brightness limits of the explored Galactic cirri regions.
2. We find no optical diffuse emission without a far IR counterpart, at least down to $28.5\text{ mag arcsec}^{-2}$ (g band). Consequently, all the highly extended diffuse emission present in the optical data can be considered due to Galactic dust above $28.5\text{ mag arcsec}^{-2}$ (g band).
3. Deep optical data can be used to detect Galactic cirri as well as far IR data. Optical data has the advantage of having a much better spatial resolution.

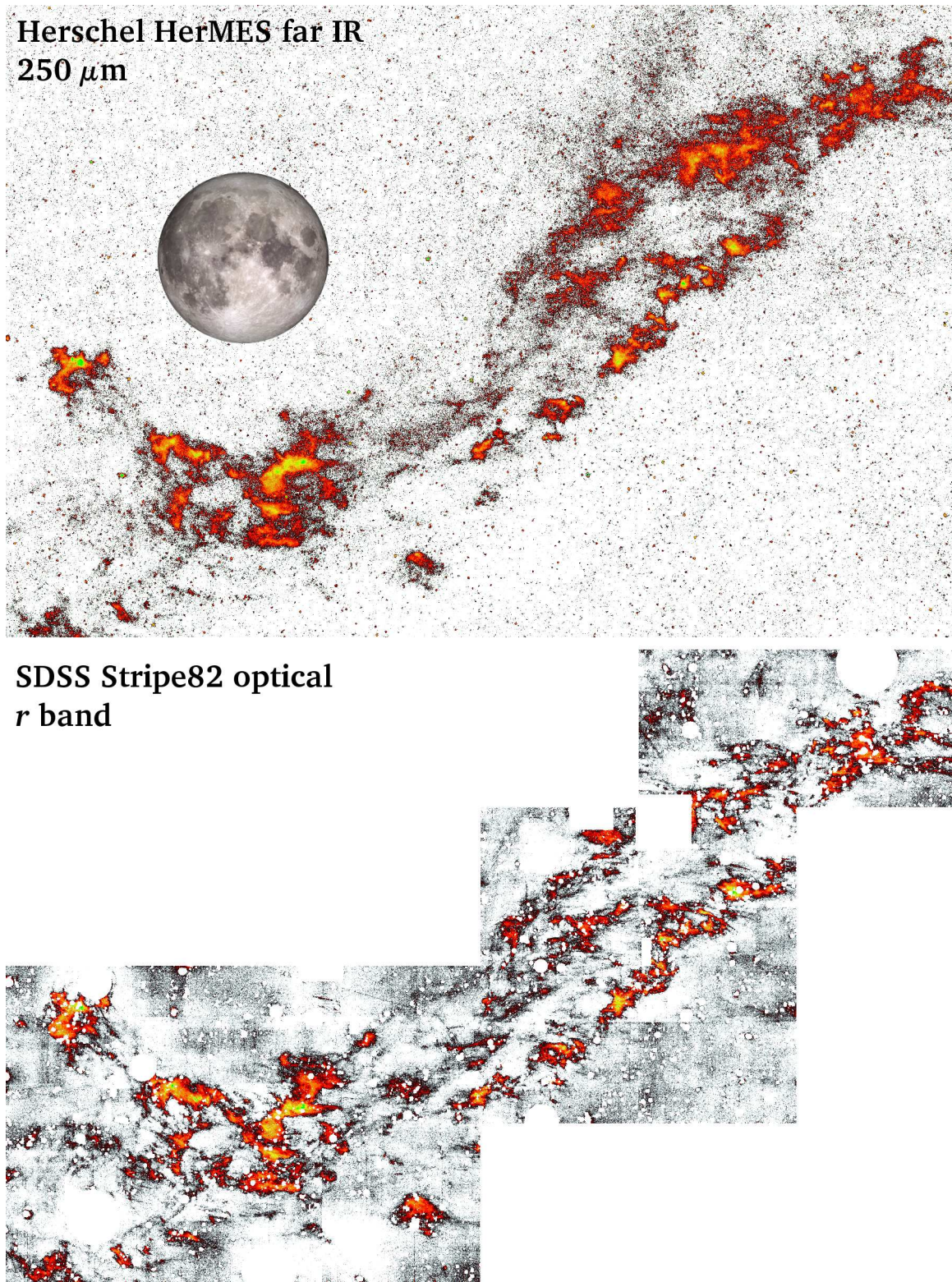


Fig. 7. The same Galactic cirrus as observed in the far IR and optical, named as "Cirrus field" (see main text). Top panel: $250 \mu\text{m}$ band from the HerMES map. Lower panel: r band from the IAC Stripe82 Legacy Survey. The pixel scale for both images is 6 arcsec. An image of the moon (31 arcmin in diameter) is placed as angular scale reference.

4. The optical colors of the Galactic cirri

The appearance of the Galactic cirrus resemble the shape and brightness of extragalactic structures, such as tidal streams or any other stellar diffuse feature in deep optical observations. It is, therefore, imperative to characterize the optical properties of

the Galactic dust aiming to identifying it against extragalactic sources. In particular, we are interested in exploring any potential difference between the optical colors of the Galactic cirri and the extragalactic sources. Assuming that the optical colors of the cirri are due to the light reflected by the surrounding stars, these colors may vary depending on the chemical composition of the

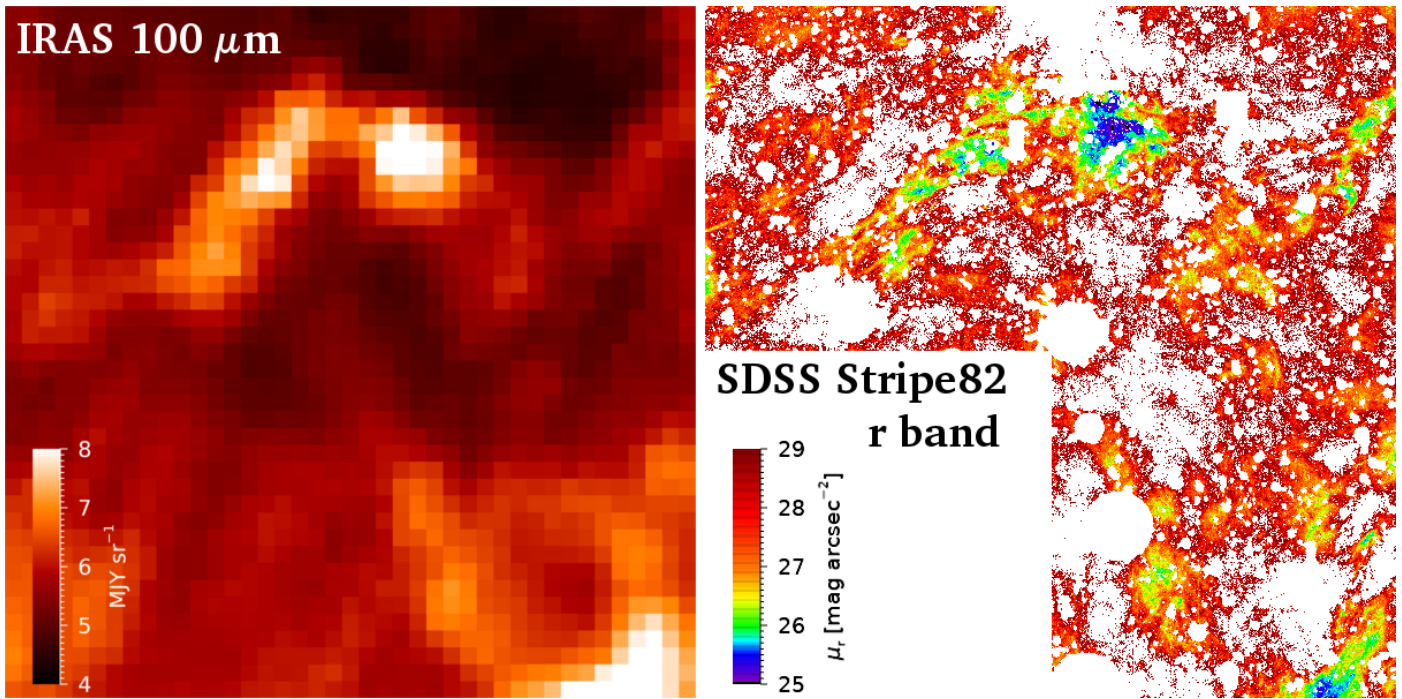


Fig. 8. IRAS 100 μm band image (left panel) and r band image (right panel) of the Field 2 presented in Table 2. Masked areas appear white in the r band. The field has dimensions of 1x1 degrees. The pixel scale is 6 arcseconds in the optical image. A region of this mosaic was used as an example of the image processing in Section 2, Fig. 4.

dust grains, the dust column density or the average colors of the surrounding stars. In order to explore possible color trends, we selected a number of fields in the Stripe82 region.

The selection of the fields was carried out using only the optical images of the IAC Stripe82 data through visual exploration. With such strategy, we wanted to avoid any potential bias towards selecting diffuse optical emission with obvious IR counterpart. The field selection was done in such a way that we assure that, together with diffuse emission, there were regions in the images to calibrate the sky background level. We also tried to select as much as possible isolated cirri, in order to avoid the photometric complexity of having several clouds in the same line of sight. In the case of having large areas (several square degrees) susceptible of analysis, we splitted the region into different fields. This was done to provide smaller fields to explore possible color trends. The fields selected under these guidelines are listed in Table 2 ranging from $\# = 1$ to 5 , and are located in the Stripe82 region between $\text{R.A.} = [324^\circ, 4^\circ]$. Additionally, we selected areas with strong optical diffuse emission in order to draw possible correlations with the dust column density. These fields are more problematic in terms of the photometric analysis due to the difficulty in the calibration of the sky background level. An extra problem comes from the residuals of the drift-scan observational mode of SDSS. The SDSS reduction pipeline fits a polynomial to the sky emission whose typical length is of the order of several arcmin. Under the presence of any diffuse emission of similar or higher spatial scale, this SDSS algorithm will tend to interpret the diffuse emission as the sky emission itself. This causes a systematic over-subtraction of the data. Nevertheless, the same sky subtraction polynomial fitting is performed in different bands. Hence, for fields with a high contamination and large extension of diffuse emission, we do not consider the absolute value of the surface brightness in each band as reliable. However, we will show that the derived colors are robust. The higher presence of optical diffuse emission is found in two re-

gions: $326^\circ < \text{R.A.} < 330^\circ$ (fields ranging from $\# = 6$ to 10) and $54^\circ < \text{R.A.} < 60^\circ$ (fields ranging from $\# = 11$ to 16). The final number of selected fields according with these criteria are 16 (including the "Cirrus Field" analyzed in the previous section as Field $\# = 5$).

All the selected fields were processed following the methodology described in Section 2, that includes the removal of the stars, masking, rebinning to 6 arcsec pixel scale and calibration of the sky background level. We compared the optical emission of the selected fields with the emission in the $100 \mu\text{m}$ IRAS band, and we always found an equivalent counterpart within the spatial resolution limits of the IRAS data. As a tracer of the dust column density we used the average emission values of the $100 \mu\text{m}$ IRAS band, listed for each field in Table 2.

4.1. Methodology for obtaining the optical colors of the cirri

Performing the photometry of extended and extremely faint sources is not a straight forward task. First, the use of specialized software to produce segmentation maps in which to perform automatic photometry of extended astronomical sources is not optimal in this case. Based on the techniques developed previously (that mask all the external sources), we consider that the remaining flux in the images is due to cirri, which will be considered as a single source. However, to obtain the colors of the cirri, the integration of the total flux in the images is not possible due to the presence of oversubtraction and sky background fluctuation regions, which would strongly alter the photometry. In addition, the low signal due to the extremely low surface brightness of the cirri should also be taken into account. Having in mind all the previous considerations, we decided to use an approach based on the color distribution of the pixels of the images.

In the case of total absence of sources, that is, purely noise, the flux distribution in each band is described by a Gaussian function due to the Poisson nature of the noise in the images,

Table 2. Selected fields for the photometric analysis of the Galactic cirri.

Field #	R.A. (J2000) [deg]	Dec. (J2000) [deg]	l [deg]	b [deg]	Area [deg ²]	$\langle g-r \rangle$ [mag]	$\langle r-i \rangle$ [mag]	$\langle i-z \rangle$ [mag]	$\langle S_{100\mu m} \rangle$ [MJy sr ⁻¹]
1	324.0	0.0	54.7	-35.8	2	0.57±0.04	0.12±0.04	0.00±0.11	3.84
2	333.0	-0.75	60.8	-43.6	0.75	0.60±0.04	0.05±0.04	0.01±0.11	5.02
3	342.75	0.25	71.4	-50.2	1.75	0.63±0.04	0.13±0.04	0.10±0.11	5.59
4	344.0	-0.25	72.3	-51.4	2	0.53±0.04	0.12±0.04	0.08±0.11	4.54
5	2.5	-0.25	100.9	-61.3	3	0.57±0.04	0.06±0.04	0.04±0.11	3.97
6	326.0	0.25	56.4	-37.4	2.0	0.57±0.04	0.17±0.04	0.11±0.11	4.04
7	327.0	0.0	56.7	-38.3	2.25	0.63±0.04	0.20±0.04	0.02±0.11	5.82
8	328.0	0.0	57.5	-39.0	2.5	0.67±0.04	0.20±0.04	0.07±0.11	6.19
9	329.0	-0.25	58.1	-40.0	1.75	0.59±0.04	0.17±0.04	0.10±0.11	5.89
10	330.0	-0.75	59.1	-40.7	0.75	0.57±0.04	0.13±0.04	0.08±0.11	5.20
11	54.95	0.50	185.6	-41.0	1.35	0.61±0.04	0.14±0.04	0.09±0.11	5.41
12	55.85	0.50	186.3	-40.3	1.35	0.69±0.04	0.15±0.04	-0.10±0.11	5.98
13	56.75	0.50	187.1	-39.6	1.35	0.73±0.04	0.18±0.04	-0.05±0.11	8.28
14	57.65	0.50	187.8	-38.9	1.35	0.72±0.04	0.17±0.04	0.01±0.11	9.01
15	58.55	0.50	188.4	-38.2	1.35	0.83±0.04	0.25±0.04	0.05±0.11	14.02
16	59.5	-0.75	190.4	-38.1	1.0	0.92±0.04	0.30±0.04	0.01±0.11	15.73

whose width defines the depth. In building a photometric color, we are performing the flux ratio between both filters and so, the color distribution is described by a Lorentzian function. However, as calculating the magnitude (i.e. applying the logarithm) of the flux values of the pixels, we are taking only the positive values of the distribution. On taking the positive values, the color distribution of the noise in the image is characterized by a Lorentzian distribution centered at $x_L = -2.5 \times \log(\sigma_{f1}) + 2.5 \times \log(\sigma_{f2})$, where σ_{f1} and σ_{f2} are the 1σ width of the distribution in counts for both bands respectively. In other words, the center of the color distribution (in the AB system) is defined by the difference in depth between both bands.

In our case, the color distribution in the images is a combination of noise and the intrinsic color of the cirri. The color distribution of the cirri is, in principle, unknown. A good approximation is to assume that it is described by a Gaussian distribution. This gaussianity would appear as the result of intrinsic color variations of the dust combined with random noise. Following this approach, we fitted the color distribution of the pixels within an image with a Lorentzian plus a Gaussian function:

$$f(x) \equiv I_L \frac{\frac{1}{2}\Gamma}{(x - x_L)^2 + (\frac{1}{2}\Gamma)^2} + I_g \exp\left(-\frac{(x - x_g)^2}{2\sigma^2}\right)$$

Where x is the given optical color and $\{I_L, \Gamma, x_L\}$, $\{I_g, \sigma, x_g\}$ are the intensity, width and center of the Lorentzian and Gaussian functions respectively. Thus, the resulting x_g will give the average color value of the dust in the analyzed field. As discussed above, the Gaussian width (σ) will account for intrinsic color variations of the dust. For that reason, the color obtained by this technique must be considered as an average color in the analyzed area. We tested this approach through simulations carried out in the Control Field (no presence of dust). We injected structures of known colors and similar surface brightness to that of the typical cirri analyzed in this work. These simulations show the accuracy in the recovery of the cirri colors using this method. We estimated the following photometric errors: $\Delta(g-r) = 0.04$ mag, $\Delta(r-i) = 0.04$ mag and $\Delta(i-z) = 0.11$ mag. We describe these simulations and further details of the method in the Appendix C.

In Fig. 9 we show our analysis applied to the Cirrus field (# 5 in Table 2). In the right panels, we plot the color histograms of pixels for $g-r$, $r-i$ and $i-z$. Overplotted to the histograms are

the fits to the distributions using a combination of a Lorentzian plus a Gaussian functions (purple color). The Lorentzian (red) and Gaussian (blue) separated distributions are also plotted to show their relative contribution. As can be observed, the color distributions are very well described with the combination of a Lorentzian plus a Gaussian distributions. We found that in the case of the $i-z$ color, there is a slight deviation with respect to the fitting function due to the shallower z band and its higher sky fluctuations. Alternatively, in the left panels, we show the color vs. surface brightness distributions of the pixels. To avoid artificial correlations, the color distributions are plotted against the surface brightness of a band that is not included in the color. We represent with diamonds the average color values in surface brightness bins of 0.5 mag arcsec⁻². As expected, the color of brighter pixels is dominated by the typical color of the Cirrus under study (dashed blue line). As we move to fainter regions or pixels, we find a transition to a color dominated by the color of the noise (dashed red line). In the case of the $g-r$ color distribution, both the typical color of the cirrus and the color of the noise are very similar and the transition between both regimes can not be well appreciated. The dust colors in this particular field are $g-r = 0.57 \pm 0.04$ mag, $r-i = 0.06 \pm 0.04$ mag and $i-z = 0.04 \pm 0.11$ mag. It should be noted that these colors agree with the two-dimensional color maps of this cirrus field shown in Appendix D and the trends observed in Fig 6.

Finally, we performed the described methodology to all the fields. In Table 2 we summarize the properties of these fields together with the obtained optical colors. The total area analyzed is 26.5 square degrees, which corresponds roughly to 10% of the whole IAC Stripe82 Legacy Survey area.

4.2. Optical color trends of the Galactic cirri

In this section, we explore the color trends of the Galactic Cirri based on their infrared emission. Using the IRAS 100 μm intensity map, we calculated the average IR emission as a proxy of the dust column density in the selected fields. This average value is calculated taking into account the masked regions of the optical fields. As discussed previously, the errors in the measurement of the average optical color of the cirri in the selected fields are $\Delta(g-r) = 0.04$ mag, $\Delta(r-i) = 0.04$ mag and $\Delta(i-z) = 0.11$ mag. The error for the average value of the 100 μm emission is negligible, due to the large number of pixels to average that value

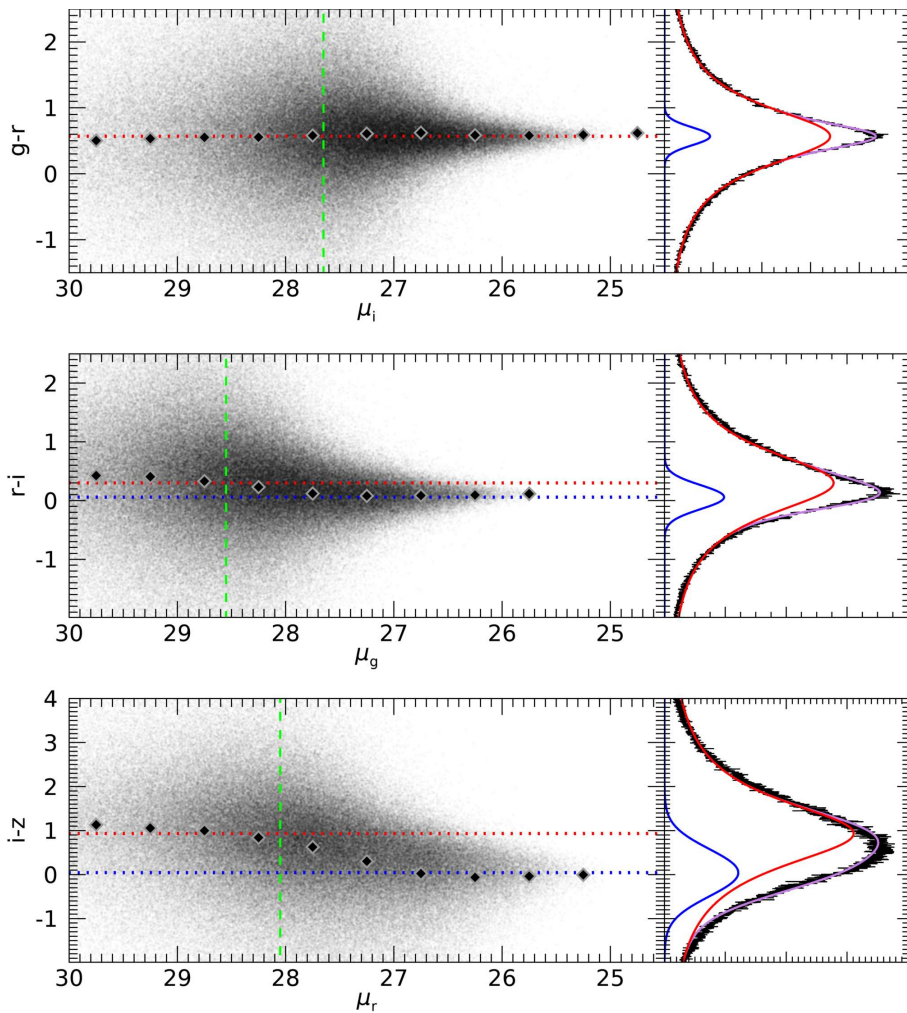


Fig. 9. Visual representation of the methodology for obtaining the colors of the Cirrus field. Left panels show the color vs. surface brightness distribution of the pixels (6 arcsec width). The black diamonds represent the average color in surface brightness bins of 0.5 mag arcsec⁻². The green dashed line marks the 3σ detection limit of the band in the x-axis. The blue and red dotted lines mark the center of the Gaussian and Lorentzian fitted functions respectively (x_g and x_L). Right panels correspond to the color distribution histograms. The black line shows the observed color distribution. The purple line shows the Gaussian plus Lorentzian fitted function, while the blue and red lines show the Gaussian and Lorentzian functions independently.

in the selected fields: $\Delta(< S_{100\mu m} >) = \sigma / \sqrt{N} \approx 0$. We plot in Fig. 10 the correlation between the $100\mu m$ emission and the optical colors of the Galactic cirri for the selected fields. We find a clear correlation between the dust column density as traced by the far IR emission and the optical colors, being steeper for the bluer optical colors. We do not find any obvious trend between the far IR emission and the $i-z$ color within the error bars. To explore any potential trend of the dust colors with the position in the sky, we separate the different fields by coordinates. Fields with right ascension ranging between 324 deg to 2.5 deg (fields # 1 to 10) are plotted with a blue symbol. Fields with a right ascension ranging between 54 deg to 60 deg (fields # 11 to 16) are plotted with a red symbol. We do not find any obvious trend in this correlation as a function of the right ascension coordinates.

As an additional analysis, we plot in Fig. 11 the optical colors of the cirri vs. their celestial coordinates in right ascension and galactic latitude and longitude. We did not conduct this analysis for the declination because the Stripe82 region subtends a narrow declination range of -2.5 deg to 2.5 deg. For comparison, we also plot the average $100\mu m$ emission. We do not find any trend between the cirri colors and the celestial coordinates within the

explored regions, being the color variations of the cirri linked to the emission in the $100\mu m$ IRAS band.

4.3. Dust vs. extragalactic features colors

The goal of this work is to explore whether there is any potential difference between the optical colors of the Galactic dust and extragalactic sources. In Fig. 12, we plot the measured colors of the cirri in the selected fields together with the colors from the E-MILES single stellar population models (Vazdekis et al. 2016) for different ages and metallicities. We also include the colors of real extragalactic sources in the images. For this, we used the dust-free Control field discussed in Section 3 and we selected pixels belonging to galaxies (sources with stellarity parameter less than 0.2) in the original images at the original pixel scale of 0.396 arcseconds. The color of the galaxies is shown as the contour regions in the color-color maps. We plotted the 1σ and 2σ density contours. Note that the average colors of real extragalactic sources differ slightly from that of single stellar population models due to the non evaluated k-correction of sources at different redshifts. Additionally, the relatively high dispersion

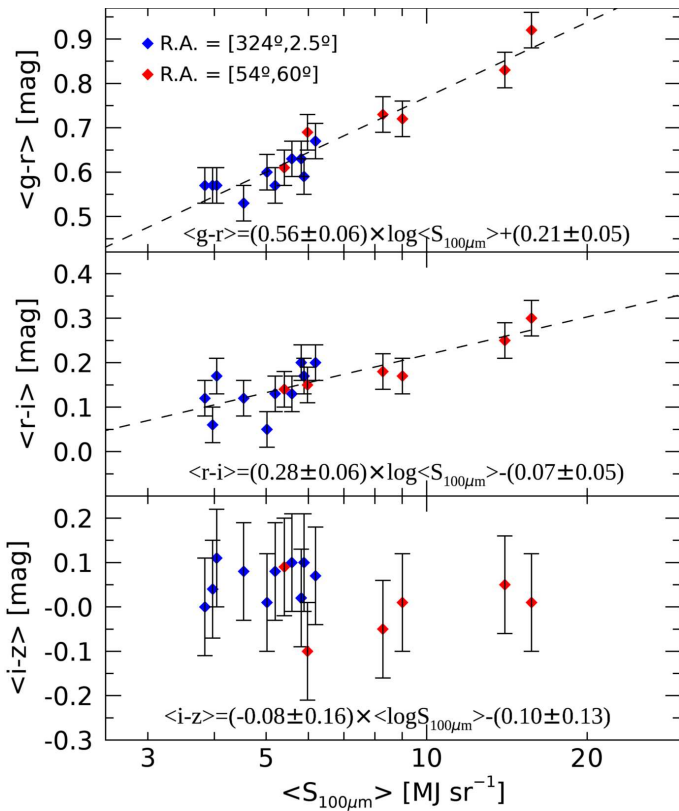


Fig. 10. Correlation between the average optical colors of the cirri and the average far IR emission in the $100\mu\text{m}$ IRAS band. The blue and red diamonds represent fields within different right ascension regions as described in the upper left corner. The error bars show the photometric uncertainty for the optical colors. The dashed lines are the best fits as indicated in the bottom equation of each panel.

found is consequence of: 1) the presence of multiple stellar populations in real galaxies, 2) the photometry using the original pixel scale of 0.396 arcsec (the cirri colors were obtained averaging its emission at larger regions) and 3) the redshift scatter.

While for the $r-i$ vs $i-z$ map the colors of the cirri overlap with the colors of the single stellar population models and real observed galaxies, for the $g-r$ vs $r-i$ and $g-r$ vs $i-z$ diagrams, the colors of the cirri are well differentiated from the single stellar population models and the real extragalactic sources. It is worth mentioning the shallower depth of the z -band translates into a greater uncertainty of the $i-z$ color. Therefore, the optical colors appears as a potential tool to break the confusion between Galactic dust and extragalactic sources.

5. Conclusions and discussion

We have carried out a comprehensive study of the Galactic cirri within the Stripe82 region using data from the IAC Stripe82 Legacy Survey (Fliri & Trujillo 2016). Through a detailed characterization of the PSF and using custom made techniques specially designed for studying deep optical data, we have demonstrated that it is possible to characterize the optical colors of the diffuse emission of interstellar dust. Both the subtraction of the scattered light from the stars and a correct masking of all the sources are essential for a correct analysis of the dust clouds. We analyzed a total area of 26.5 square degrees. We found a spatial correspondence between the optical emission and the emission of the dust cold component as traced by the far IR bands in Her-

schel and IRAS bands. Additionally, we did not find any source of optical diffuse emission without an IR counterpart.

The techniques developed in this work allow to accurately measure the average colors of the Galactic cirri in areas of few square degrees. We found a strong correlation between the average optical colors and the $100\mu\text{m}$ band average emission. This correlation is steeper for the $g-r$ color than for the $r-i$ color. We did not find such a correlation for the $i-z$ color within the photometric uncertainties, much higher for the shallower z band. The correlation between the cirri optical colors and the dust column density is a remarkable result that has not been identified previously (see a summary of previous works by Ienaka et al. 2013, Table 3). The previous lack of detection of these correlations could be related with the presence of the scattered light by the stars. In this work, this source of contamination has been carefully subtracted.

An interesting exercise would be to compare our measured colors in highly contaminated regions by dust with the spectrum of the diffuse Galactic light provided by Brandt & Draine (2012). This spectrum was calculated by averaging SDSS sky spectra in areas with $S_{100\mu m} > 10 \text{ MJy sr}^{-1}$. When convolving this spectrum with the SDSS filter response, we obtain the following colors: $g-r = 0.84 \text{ mag}$ and $r-i = 0.34 \text{ mag}$, therefore, compatible with our findings (see Fig. 10), giving reliability to our results.

It is worth exploring which physical mechanisms are able to produce such a correlation between the optical color and the far IR emission for the Galactic dust, as shown in Fig. 10. It could be related with processes of self-extinction and scatter of photons along the line of sight. A naive scenario is that the reflected optical light from a given dust cloud could be suffering extra extinction (and so, extra reddening) if there is an additional dust component along the line of sight. Therefore in areas with a higher dust column density, the colors would become redder. In fact, the extinction values of the field with the highest presence of dust analyzed in this work (Field # = 16), are $A^c(g-r) = 0.43 \text{ mag}$, $A^c(r-i) = 0.25 \text{ mag}$ and $A^c(i-z) = 0.18 \text{ mag}$ (Schlafly & Finkbeiner 2011) are of the same order (but slightly higher) than the difference in color between this field and less contaminated fields, as expected in this scenario. Additionally, the blue colors of the cirri found by Mihos et al. (2017) in the Virgo Cluster (where the dust contamination by cirri is moderate) and the redder colors found by Watkins et al. (2016) in a conspicuous and dense cloud near the M64 galaxy (where the dust contamination by cirri is severe) are in general terms compatible with this scenario. Note that these works performed a subtraction of the scattered light by the stars, as we did in this work.

In order to inquire more on the scenario stated above, we show in Fig. 13 a field that can add some light to this discussion. The field depicted in Fig. 13 contains a conspicuous cloud with a high far IR emission (high column density) adjacent to a fairly clean area (right part of the image) in which the sky can be calibrated accurately. The colors of the cirri in this area are compatible with the correlation previously shown ($S_{100\mu m} = 14.1 \text{ MJy sr}^{-1}$, $g-r = 0.75$, $r-i = 0.23$, $i-z = 0.01$)³. This field presents a very peculiar configuration. In the central upper part of the image there is what looks like a star in the vicinity of the dust screen, illuminating it directly. This low-brightness nebula was previously catalogued as a low-surface-brightness galaxy by (Impey et al. 1996, the 0351-0019 galaxy), however, in our deeper data it seems to be a bright reflection on the dust by an adjacent star. To obtain the colors of this reflection, we subtract the

³ This suggests that the colors obtained in other highly contaminated regions without a clear zero sky reference are accurate (see Sec. 4)

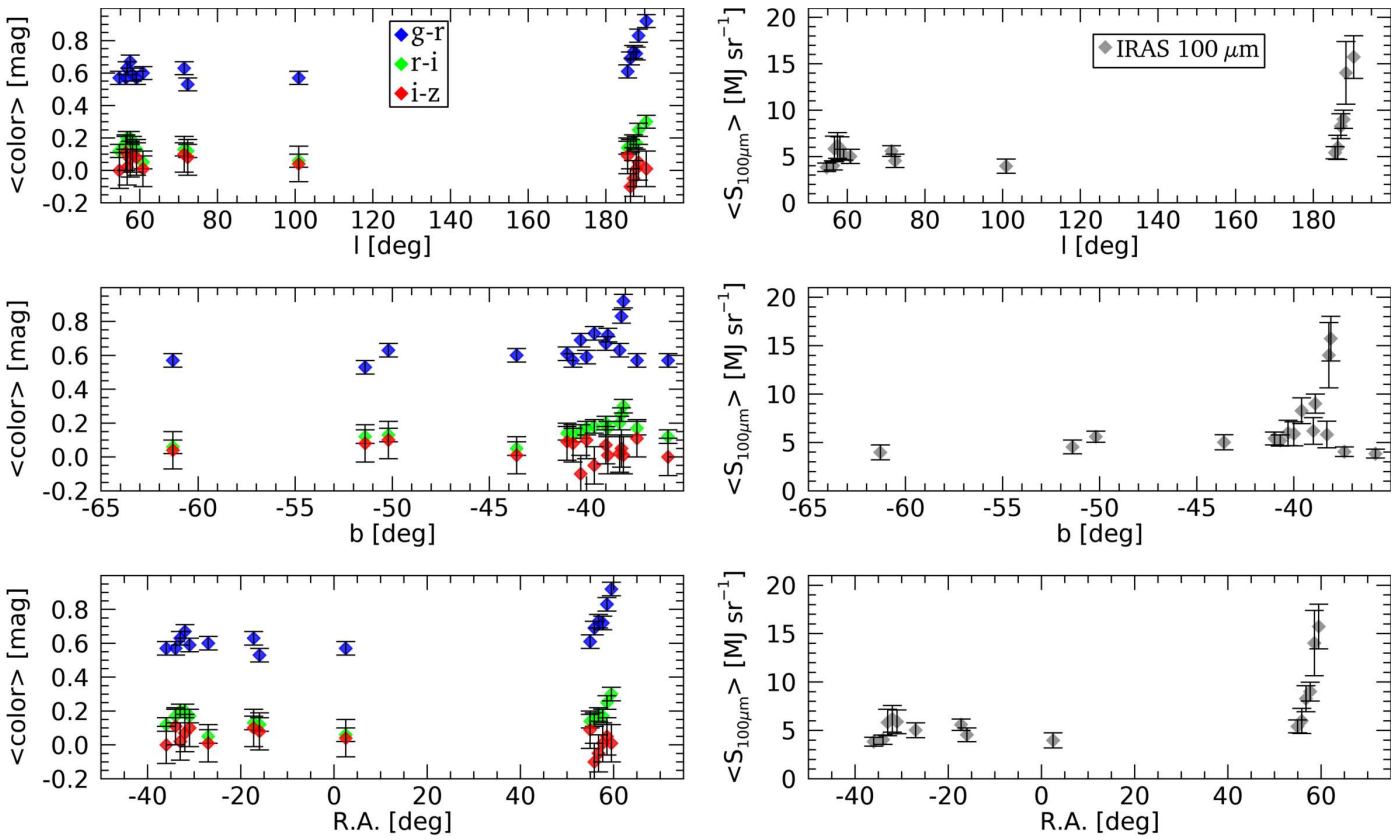


Fig. 11. Left panel: Optical colors of the cirri as a function of the location in the sky. Right panel: Same as in the left panel but showing the emission in the IRAS 100 μm band as comparison.

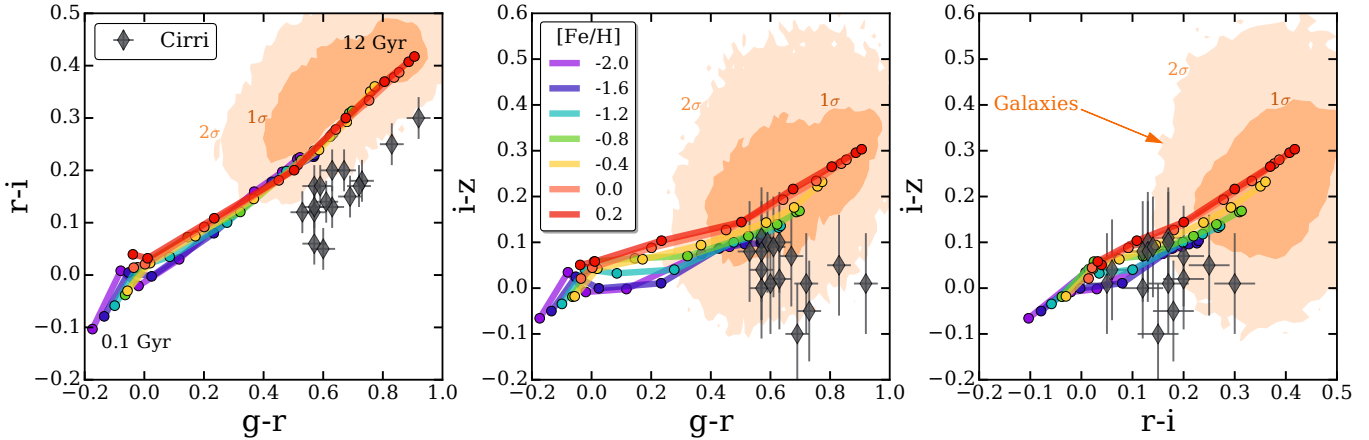


Fig. 12. Color-color diagrams of the Galactic cirri and the extragalactic sources. Black/grey diamonds correspond to the cirri colors with their corresponding error bars. Overplotted are E-MILES single stellar population models color-coded for different metallicities at each of the following ages: 0.1, 0.2, 0.5, 1, 2, 5, 10 and 12 Gyr. We also plot the color values of the pixels of real galaxies (see text). The light orange region encloses 95% (2 σ) of the pixels, while the dark orange encloses 68% (1 σ).

star using the PSF in a similar way to that described in previous sections. Additionally, with this methodology, we are able to obtain the flux of the star, that being saturated, is the only way to obtaining it. The resulting colors of the star are $g-r = 0.51$, $r-i = 0.21$, $i-z = 0.20$. To obtain the color of the nebula, we selected a small region, avoiding the central area where the inner internal reflection could affect the obtained colors. As the area subtended by the nebula is small, we work at the original pixel scale of 0.396 arcsec of the image. This also prevent us of ob-

taining its colors in a similar fashion to that of the wide regions, as described in the previous section. At this spatial resolution, the signal to noise of the z band is low, therefore we discard this band for this analysis. The colors of the nebula are $g-r \approx 0.25$ and $r-i \approx 0.10$. The fact that the nebula has colors considerably bluer than the adjacent star suggests a dust albedo that causes a bluing of the reflected light. Additionally, the observed red dust colors in the surrounding field and the observed blue colors of the dust directly illuminated by the star supports the scenario of self

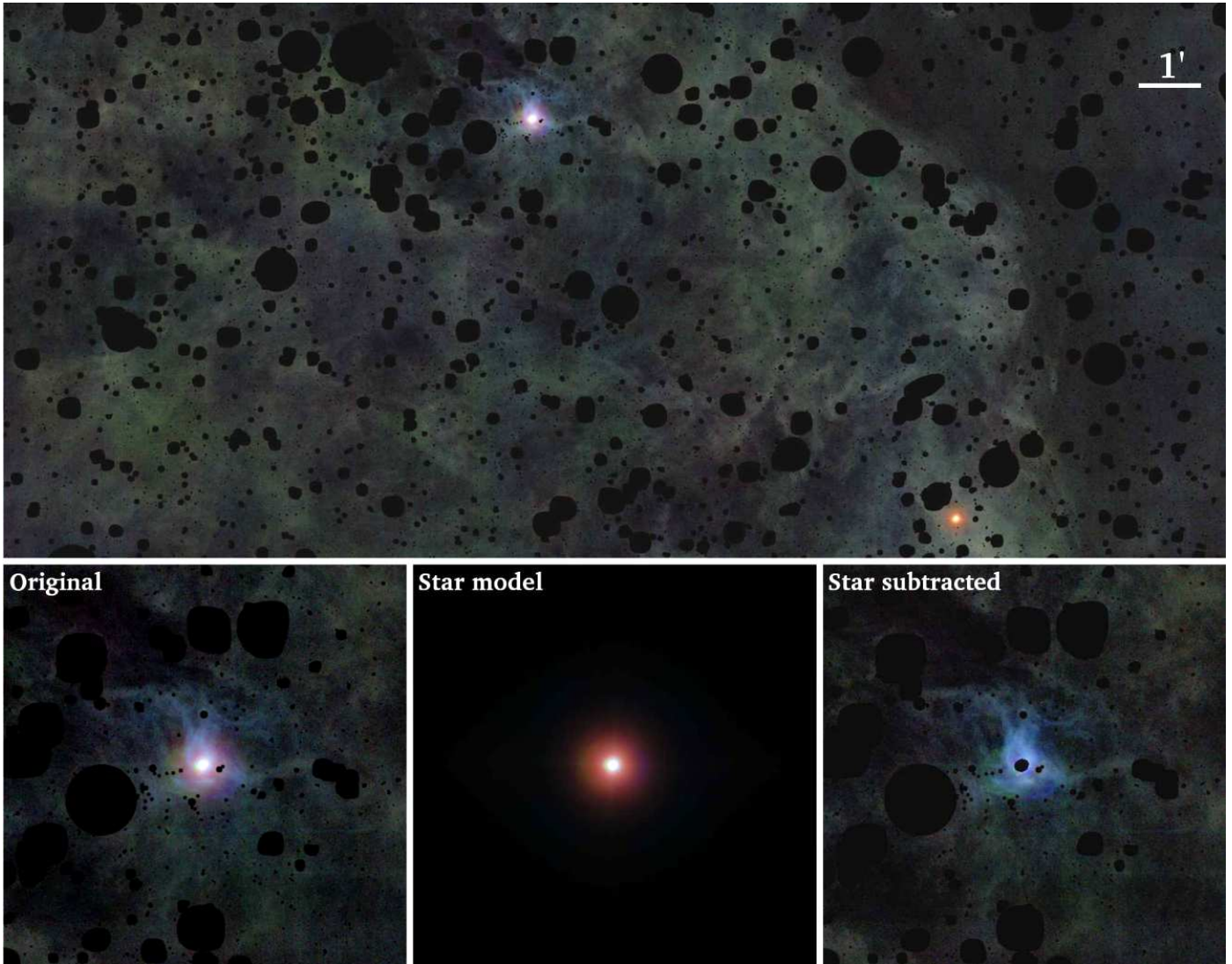


Fig. 13. Composite color image using g , r and i SDSS bands of the region RA = [58.1, 58.8], Dec = [-0.4, -0.1] at a pixel scale of 0.396 arcsec. All the sources have been masked / subtracted except the star that appears directly illuminating the dust screen and a random star in the bottom right side illustrating the appearance of all the stars without this fact. In the lower panels a zoom of 6.5×6.5 arcmin of the area of interest is shown with the result of the subtraction of the star, showing more clearly the reflected area.

extinction, in which the light reflected (without going through several dust curtains) is bluer and the light going through dense dust is strongly scattered in the blue bands, and therefore, observed redder. The scenario depicted here would be a simple and feasible explanation to the extended red emission found in some dense cirri regions (e.g. Witt et al. 2008).

Finally, it is also worth briefly discussing the potential of different optical surveys in the study of Galactic dust. In this work, we have used data from the IAC Stripe82 Legacy Survey to study wide regions with presence of dust. The imminent arrival of the LSST could be extremely useful in the study of the photometric properties of the Galactic dust. The presence of six photometric bands (u , g , r , i , z and y), the great depth of the final coadded data and the large explored area (30,000 square degrees of sky) are excellent characteristics for the detection and characterization of the Galactic dust. However, without an excellent reduction of the data preserving low surface brightness sources, and an exquisite characterization of the PSF at large radius to model and subtract the scattered field by stars, the study of extended diffuse emission will be compromised. Assuming that the

final images meet the quality required to study the optical diffuse emission, it could be possible to conduct a systematic study of the Galactic dust using this superb optical dataset. The main advantage with respect to surveys in the far IR will be the much better spatial resolution and depth. This would allow to trace the dust and create extinction maps with an unprecedented quality. Note that the use of other wavelengths for the detection of dust with a higher spatial resolution have already been proposed, for example by Boissier et al. (2015) using data in the UV, which could be complementary to the optical data of the LSST.

Acknowledgements. The authors of this paper acknowledge support from grant AYA2016-77237-C3-1-P from the Spanish Ministry of Economy and Competitiveness (MINECO). We acknowledge support from the Fundación BBVA under its 2017 programme of assistance to scientific research groups, for the project "Using machine-learning techniques to drag galaxies from the noise in deep imaging". We thank Timothy Brandt for sharing the spectrum of the diffuse galactic light with us. We thank Jorge Sánchez Almeida and David Valls-Gabaud for interesting discussions about the results. We thank Aaron Watkins for complementary analysis about the galactic dust colors and Juergen Fliri for his excellent work on the construction of the IAC Stripe82 Legacy Survey. We thank Lee Kelvin for sharing his code to compute beautiful color composed images. JR thanks Anastasia Khamatullina for interesting discussions. We also thank the

participants of the workshop "Exploring the Ultra-Low Surface Brightness Universe" hosted in the ISSI headquartes, Bern, Switzerland on January 2017, Bern, Switzerland in which preliminary result were shown. JR thanks MINECO for financing his PhD through FPI grant. I.T. acknowledges financial support from the European Union's Horizon 2020 research and innovation programme under Marie Skłodowska-Curie grant agreement No 721463 to the SUNDIAL ITN network. This research has been partly supported by the Spanish Ministry of Economy and Competitiveness (MINECO) under grants AYA2016-77237-C3-1-P.

References

- Abraham, R. G., & van Dokkum, P. G. 2014, PASP, 126, 55
- Abadi, M. G., Navarro, J. F., & Steinmetz, M. 2006, MNRAS, 365, 747
- Abazajian, K. N., Adelman-McCarthy, J. K., Agüeros, M. A., et al. 2009, ApJS, 182, 543-558
- Aihara, H., Arimoto, N., Armstrong, R., et al. 2018, PASJ, 70, S4
- Akhlaghi, M., & Ichikawa, T. 2015, ApJS, 220, 1
- Barrena, R., Streblyanska, A., Ferragamo, A., et al. 2018, A&A, 616, A42.
- Bertin, E., & Arnouts, S. 1996, A&AS, 117, 393
- Bertin, E., Mellier, Y., Radovich, M., et al. 2002, Astronomical Data Analysis Software and Systems XI, 281, 228
- Bertin, E. 2011, Astronomical Data Analysis Software and Systems XX, 442, 435
- Besla, G., Martínez-Delgado, D., van der Marel, R. P., et al. 2016, ApJ, 825, 20
- Bílek, M., Cuillandre, J.-C., Gwyn, S., et al. 2016, A&A, 588, A77
- Blanton, M. R., Lupton, R. H., Schlegel, D. J., et al. 2005, ApJ, 631, 208
- Boissier, S., Boselli, A., Voyer, E., et al. 2015, A&A, 579, A29
- Borlaff, A., Trujillo, I., Román, J., et al. 2019, A&A, 621, A133.
- Brandt, T. D., & Draine, B. T. 2012, ApJ, 744, 129
- Bullock, J. S., & Johnston, K. V. 2005, ApJ, 635, 931
- Chiboucas, K., Karachentsev, I. D., & Tully, R. B. 2009, AJ, 137, 3009
- Chiboucas, K., Jacobs, B. A., Tully, R. B., & Karachentsev, I. D. 2013, AJ, 146, 126
- Cooper, A. P., Cole, S., Frenk, C. S., et al. 2010, MNRAS, 406, 744
- Cooper, A. P., Gao, L., Guo, Q., et al. 2015, MNRAS, 451, 2703
- Cortese, L., Bendo, G. J., Isaak, K. G., Davies, J. I., & Kent, B. R. 2010, MNRAS, 403, L26
- Dalcanton, J. J., Spergel, D. N., Gunn, J. E., Schmidt, M., & Schneider, D. P. 1997, AJ, 114, 635
- Dark Energy Survey Collaboration, Abbott, T., Abdalla, F. B., et al. 2016, MNRAS, 460, 1270
- Das, S., Louis, T., Nolta, M. R., et al. 2014, J. Cosmology Astropart. Phys., 4, 014
- Duc, P.-A., Cuillandre, J.-C., & Renaud, F. 2018, MNRAS, 475, L40.
- de Jong, R. S. 2008, MNRAS, 388, 1521
- de Vries, C. P., & Le Poole, R. S. 1985, A&A, 145, L7
- DeVore, J. G., Kristl, J. A., & Rappaport, S. A. 2013, Journal of Geophysical Research (Atmospheres), 118, 5679
- Davies, J. I., Wilson, C. D., Auld, R., et al. 2010, MNRAS, 409, 102
- Duc, P.-A., Cuillandre, J.-C., Karabal, E., et al. 2015, MNRAS, 446, 120
- Elvey, C. T., & Roach, F. E. 1937, ApJ, 85, 213
- Erwin, P. 2015, ApJ, 799, 226
- Ferrarese, L., Côté, P., Cuillandre, J.-C., et al. 2012, ApJS, 200, 4
- Fliri, J., & Trujillo, I. 2016, MNRAS, 456, 1359
- Giallongo, E., Menci, N., Grazian, A., et al. 2014, ApJ, 781, 24
- Guhathakurta, P., & Tyson, J. A. 1989, ApJ, 346, 773
- Henyey, L. G., & Greenstein, J. L. 1941, ApJ, 93, 70
- Hodges-Kluck, E., & Bregman, J. N. 2014, ApJ, 789, 131
- Ibata, R., Mouhcine, M., & Rejkuba, M. 2009, MNRAS, 395, 126
- Ibata, R. A., Lewis, G. F., McConnachie, A. W., et al. 2014, ApJ, 780, 128
- Ienaka, N., Kawara, K., Matsuoka, Y., et al. 2013, ApJ, 767, 80
- Impey, C., Bothun, G., & Malin, D. 1988, ApJ, 330, 634
- Impey, C. D., Sprayberry, D., Irwin, M. J., & Bothun, G. D. 1996, ApJS, 105, 209
- Infante-Saiz, R., Trujillo I., Román J., 2019, in preparation.
- Javanmardi, B., Martinez-Delgado, D., Kroupa, P., et al. 2016, A&A, 588, A89
- Johnston, K. V., Bullock, J. S., Sharma, S., et al. 2008, ApJ, 689, 936-957
- Karabal, E., Duc, P.-A., Kuntschner, H., et al. 2017, A&A, 601, A86
- Klypin, A., Kravtsov, A. V., Valenzuela, O., & Prada, F. 1999, ApJ, 522, 82
- Lamarre, J. M., Puget, J. L., Bouchet, F., et al. 2003, New A Rev., 47, 1017
- Laureijs, R. J., Mattila, K., & Schnur, G. 1987, A&A, 184, 269
- Levenson, L., Marsden, G., Zemcov, M., et al. 2010, MNRAS, 409, 83
- Low, F. J., Young, E., Beintema, D. A., et al. 1984, ApJ, 278, L19
- Lu, T., Luo, W., Zhang, J., et al. 2018, AJ, 156, 14.
- LSST Science Collaboration, Abell, P. A., Allison, J., et al. 2009, arXiv:0912.0201
- Martin, N. F., Ibata, R. A., Rich, R. M., et al. 2014, ApJ, 787, 19
- Martínez-Delgado, D., Gabany, R. J., Crawford, K., et al. 2010, AJ, 140, 962
- Mattila, K. 1979, A&A, 78, 253
- McConnachie, A. W., Irwin, M. J., Ibata, R. A., et al. 2009, Nature, 461, 66
- McConnachie, A. W. 2012, AJ, 144, 4
- McConnachie, A. W., Ibata, R., Martin, N., et al. 2018, ApJ, 868, 55
- Mihos, J. C., Harding, P., Feldmeier, J., & Morrison, H. 2005, ApJ, 631, L41
- Mihos, J. C., Durrell, P. R., Ferrarese, L., et al. 2015, ApJ, 809, L21
- Mihos, J. C., Harding, P., Feldmeier, J. J., et al. 2017, ApJ, 834, 16
- Mihos, J. C., Carr, C. T., Watkins, A. E., Oosterloo, T., & Harding, P. 2018, ApJ, 863, L7
- Miville-Deschénes, M.-A., & Lagache, G. 2005, ApJS, 157, 302
- Monet, D. G., Levine, S. E., Canzian, B., et al. 2003, AJ, 125, 984
- Montes, M., & Trujillo, I. 2014, ApJ, 794, 137.
- Montes, M., & Trujillo, I. 2018, MNRAS, 474, 917
- Moore, B., Ghigna, S., Governato, F., et al. 1999, ApJ, 524, L19
- Muslimov, E., Valls-Gabaud, D., Lemaître, G., et al. 2017, Appl. Opt., 56,
- Pilbratt, G. L., Riedinger, J. R., Passvogel, T., et al. 2010, A&A, 518, L1
- Planck Collaboration, Ade, P. A. R., Aghanim, N., et al. 2011, A&A, 536, A19
- Peacock, M. B., Strader, J., Romanowsky, A. J., & Brodie, J. P. 2015, ApJ, 800, 13
- Ramírez-Moreta, P., Verdes-Montenegro, L., Blasco-Herrera, J., et al. 2018, A&A, 619, A163.
- Román, J., & Trujillo, I. 2018, Research Notes of the American Astronomical Society, 2, 144
- Rudick, C. S., Mihos, J. C., Harding, P., et al. 2010, ApJ, 720, 569
- Sandage, A. 1976, AJ, 81, 954
- Sandage, A., & Binggeli, B. 1984, AJ, 89, 919
- Sandin, C. 2014, A&A, 567, A97
- Schlafly, E. F., & Finkbeiner, D. P. 2011, ApJ, 737, 103
- Slater, C. T., Harding, P., & Mihos, J. C. 2009, PASP, 121, 1267
- Sollima, A., Gil de Paz, A., Martínez-Delgado, D., et al. 2010, A&A, 516, A83
- Tanaka, M., Chiba, M., Komiyama, Y., Guhathakurta, P., & Kalirai, J. S. 2011, ApJ, 738, 150
- Thacker, C., Cooray, A., Smidt, J., et al. 2013, ApJ, 768, 58
- Trujillo, I., & Fliri, J. 2016, ApJ, 823, 123
- Uson, J. M., Boughn, S. P., & Kuhn, J. R. 1991, ApJ, 369, 46
- Valls-Gabaud, D., & MESSIER Collaboration 2017, Formation and Evolution of Galaxy Outskirts, 321, 199
- Vazdekis, A., Koleva, M., Ricciardelli, E., Röck, B., & Falcón-Barroso, J. 2016, MNRAS, 463, 3409
- Veneziani, M., Ade, P. A. R., Bock, J. J., et al. 2010, ApJ, 713, 959
- Viero, M. P., Wang, L., Zemcov, M., et al. 2013, ApJ, 772, 77
- Viero, M. P., Asboth, V., Roseboom, I. G., et al. 2014, ApJS, 210, 22
- Watkins, A. E., Mihos, J. C., Harding, P., et al. 2014, ApJ, 791, 38.
- Watkins, A. E., Mihos, J. C., & Harding, P. 2015, ApJ, 800, L3.
- Watkins, A. E., Mihos, J. C., & Harding, P. 2016, ApJ, 826, 59
- Watkins, A. E., Mihos, J. C., & Harding, P. 2017, ApJ, 851, 51.
- Watkins, A. E., Mihos, J. C., Bershadsky, M., et al. 2018, ApJ, 858, L16.
- Willman, B. 2010, Advances in Astronomy, 2010, 285454
- Witt, A. N., Friedmann, B. C., & Sasseen, T. P. 1997, ApJ, 481, 809
- Witt, A. N., Mandel, S., Sell, P. H., Dixon, T., & Vijh, U. P. 2008, ApJ, 679, 497
- Zackrisson, E., de Jong, R. S., & Micheva, G. 2012, MNRAS, 421, 190

Appendix A: Surface brightness limits of the data

We describe the process for obtaining the surface brightness limits of the data. In Fig. A.1 is shown the histogram of counts of a masked image of the IAC Stripe 82 Legacy Survey for all the u , g , r , i and z bands. As can be seen, the distributions follow an almost perfect gaussian shape as all the non masked pixels are dominated by the Poisson noise of the data. This Poisson noise is what limits the depth of the data. Fitting a gaussian function we obtain its standard deviation (σ). Therefore, the surface brightness limit at the 3σ level in pixel to pixel variation can be defined as:

$$\mu_{lim}(3\sigma_{pix \times pix}) = -2.5 \times \log\left(\frac{3\sigma}{pix^2}\right) + Zp$$

where pix is the pixel size in arcseconds and Zp is the zero point of the data. In other words, this is the detection threshold in surface brightness at 3σ for a source with an angular size equivalent to that pixel size. However, the typical size of celestial sources is considerably larger. For this reason, the limiting surface brightness at the original pixel scale is not representative of the real detection threshold for extended sources. In addition, each particular survey has its own pixel scale, so this value is not comparable among different surveys or datasets. To obtain the surface brightness limit at any given angular scale, the above histograms of counts have to be obtained at the required angular scale. It could be done by rebinning the image and obtaining the standard deviation of this new distribution. However, the residuals of the masking process after the rebinning and the substantial reduction in the number of spatial elements make this option problematic, specially in images with high contamination or small area. Consequently, the practical way to obtain the surface brightness limit at a given angular scale is assuming that the flux of the noise follows a normal distribution. Then, the Gaussian standard deviation on a different angular scale will transform as:

$$\sigma(\Omega) = \sigma \sqrt{\frac{pix^2}{\Omega^2}}$$

where Ω is the desired pixel scale box of the new definition. With it, we can define the surface brightness limit for any angular scale as:

$$\mu_{lim}(3\sigma_{\Omega \times \Omega}) = -2.5 \times \log\left(\frac{3\sigma}{pix \times \Omega}\right) + Zp$$

Traditionally, an angular scale of 10×10 arcseconds boxes has been used as representative of the typical extended source when exploring nearby galaxies. Using this definition, we obtain for the data used in this work: $\mu(3\sigma; 10'' \times 10'') = 28.0$, 29.1 , 28.6 , 28.2 and 26.6 mag arcsec $^{-2}$ for the u , g , r , i and z bands respectively. It is worth noting that the limiting depth is strongly dependent on the angular size or criteria to define it. For instance, the previous values in $\mu_{lim}(3\sigma; 10'' \times 10'')$ would transform as $\mu_{lim}(1\sigma; 10'' \times 10'') = 29.2$, 30.3 , 29.8 , 29.4 and 27.8 mag arcsec $^{-2}$ or $\mu_{lim}(1\sigma; 60'' \times 60'') = 31.1$, 32.3 , 31.7 , 31.3 and 29.8 mag arcsec $^{-2}$ for the u , g , r , i and z bands respectively.

Appendix B: PSF characterization

The quality of the modeling of the scattered light produced by the stars relies on the accuracy achieved in the characterization of the PSF and the subsequent accuracy at fitting this PSF model to the stars. Bearing this in mind, we have made a characterization of the PSF taking into account possible adverse effects that

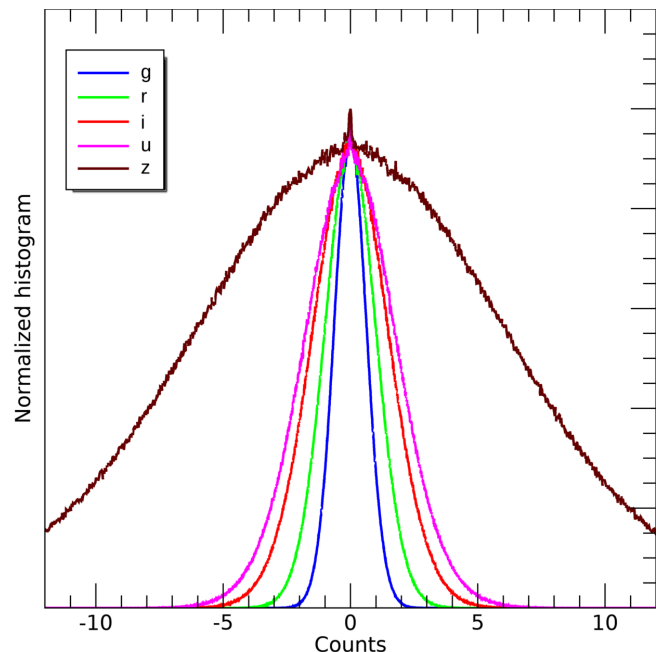


Fig. A.1. Distributions of counts for a 0.5×0.5 degrees masked image at the original pixel size of 0.396 arcsec in the five SDSS bands. The histograms in each band follow a normal distribution with a gaussian shape. All bands own a similar zero point (Z_p) of 28.3291 mag, as provided by the IAC Stripe 82 survey. Note the shallower z band evidenced by a wider distribution.

can penalize a correct PSF model. The commonly used techniques, such as dedicated observations of a very bright star, can introduce systematic effects as it is based in unique observational conditions. This could translate in a different full width at half maximum (FWHM) in the Core of the PSF, or even fluctuations of the PSF wings at large radii (DeVore et al. 2013). Additionally, this kind of "external" characterization of the PSF is not feasible to perform in data from multiple coadded surveys. The reason is that the images of the survey are the coadd of several multi-epoch single exposures, so the PSF of a single exposure could be different of the PSF in the coadded survey. Consequently, a good alternative for obtaining a high quality and realistic PSF is to use the stars in the science images themselves.

In this section, we describe the process for obtaining the PSF model used in this work. This is done by the stacking of many different stars. That "averaged star" is considered the PSF model of the data. To conduct the procedure described here, we use data from the IAC Stripe 82 Legacy Survey (Fliri & Trujillo 2016), therefore, the PSF models produced here will be those of this survey. Nevertheless, this procedure is general and can be used for any dataset of similar characteristics.

Appendix B.1: Wing PSFs

To be able to explore the effect of the scattered light at very low surface brightness, it is necessary to characterize the PSF to the largest possible spatial extent. In the present work, we have built the PSFs up to a radial distance of 720 arcseconds (12 arcmin). Such large PSFs imply that we are able to characterize and remove the scattered light down to extremely faint surface brightness. In order to maximize the reliability of the PSFs, specially at large radius, the selected stars are taken in a region with low contamination by Galactic cirri. The area chosen is the Stripe82

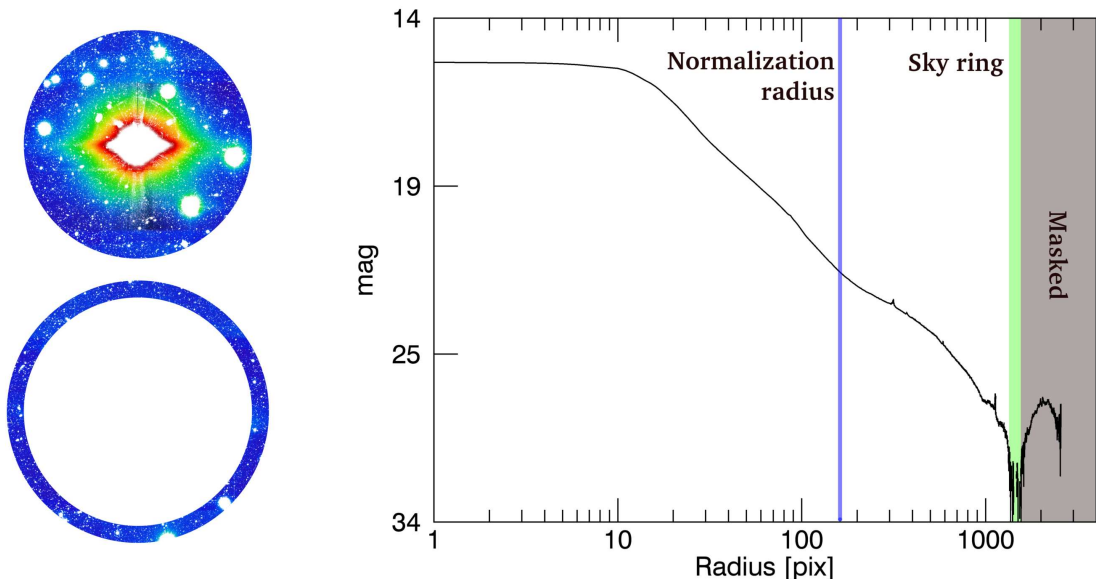


Fig. B.1. Schematic representation of the correction process for the construction of the Wing PSFs in the case of oversubtraction around very bright stars. Upper Left: An image of a very bright star which has its surrounding sky over-subtracted; Bottom left: the sky ring used to calibrate the sky that will be added to the image of the star. Right: Profile of the star showing the different regions.

region within the Hers82 survey (avoiding the cirri clouds discussed in Section 3). Due to the precision required, accurate centering of the stars is necessary. The coordinates of bright saturated stars, provided by either SDSS or by creating a catalog running SExtractor (Bertin & Arnouts 1996), do not have the desired precision. We use as central coordinates those of the USNO-B catalog of stars (Monet et al. 2003) and we select stars that have null error in the coordinates according to the USNO-B (J2000 epoch) catalogue. Stars matching this criteria in the selected area are many (≈ 1200 stars with $R < 12$ mag). However, stars with ($R < 5$ mag) are only a few. The scarcity of very bright stars forces us to stack a large number of stars in a wide range of luminosities. To combine stars with very different fluxes, we need to scale the different stars to a common flux (i.e. we need to normalize them) so they can share a common profile. The use of aperture photometry for the normalization of the individual stars is ruled out. The stars in this magnitude range are saturated in SDSS, so the flux obtained by using a fixed aperture is not reliable. For this reason we make use of the profile of each star to perform the normalization.

We proceed as follows. For each star in our pre-selected catalogue, we created an image stamp in each band with an odd number of pixels⁴ of 720 arcsec using the software SWarp (Bertin et al. 2002) centered in the coordinates of the star according to the USNO-B catalogue. We masked all the external sources based on the detection map from SExtractor using the *r-deep* band (combination of *g*, *r* and *i* bands). Then we performed a visual inspection to discard unreliable stars. Reasons for discarding a star are the presence of adjacent sources of similar luminosity, saturated rows or columns or any other artifact. Extremely bright stars are especially problematic, in fact, all stars with $R < 5$ mag were discarded. A common problem in SDSS images is the presence of ghosts in fields adjacent to bright stars. Hence, we performed a manual masking of the ghosts for each star. From our original pre-selection of 535 stars, we ended up with 399 stars in the magnitude range $5.35 < R < 10.55$, with 90% of the stars

having $R > 8$ mag and 75% $R > 9$ mag. Then, we computed the profiles for all the stars.

Another problem to handle is the oversubtraction of light around bright stars. Although the IAC Stripe82 Legacy Survey is built on the basis of preserving the lower surface brightness structures, a slight over-subtraction is detected around very bright stars. Due to the high precision required for the construction of the PSF, this must be taken into account. To minimize this issue, we developed an automatic routine in which any possible oversubtraction is corrected/softened. This is made by detecting changes in the slope of the profiles of the stars that could be indicative of oversubtraction. If oversubtraction is detected, we measured the average sky value in a ring located farthest from the star in the the oversubtracted region and we add this value back to the whole stamp. The region of the stamp with radius larger than the selected oversubtracted area is masked (see Fig. B.1 for a visual example). Then, the whole 2-D image is normalized by a multiplicative factor obtained from the flux of the star in the profile between 40 and 60 arcseconds, so each normalized star has the same flux in this region. We choose this range to avoid the central internal reflection of the star, located within the inner 40 arcseconds. We used a maximum radius of 60 arcseconds to make sure that the signal to noise ratio is reliable for the faintest stars. Once all the stars are normalized in flux we proceed with the stacking. We obtained the combined PSF averaging the 2-D images of the stars, computing the mean of each pixel with an iterative rejection based on a gaussian distribution. We rejected pixel values beyond the 2σ value. Additionally, for the low signal regions (> 300 arcseconds for the *g*, *r* and *i* bands and > 100 arcseconds for the *u* and *z* bands) we forced a minimum rejection of the 15% of the maximum and 15% of the minimum pixel values. Due to the high luminosity of the stars to construct the Wing PSFs, the inner region appears saturated. Therefore, it is necessary to construct an equivalent Core PSF to characterize this inner central region.

⁴ We use an odd number of pixels to create the PSF in order to have a central reference pixel in the 2-D final image

Appendix B.2: Core PSF They use the same PSF model everywhere?

The photometry of stars is usually based on PSFs whose size is not larger than few arcseconds. To obtain these small PSFs, the PSFEx package (PSFEx; Bertin 2011) is commonly used. However, for the construction of the inner region of our PSFs, we used a technique similar to that of the Wing PSFs, this is, the stacking of a large number of stars from the images. The stars were extracted from an area of $2.5^\circ \times 2.5^\circ$ centered at coordinates RA = 25.75, Dec. = 0. This region of the sky has a low contamination by Galactic dust, and importantly has a low number of very bright stars, therefore, low-luminosity stars are weakly influenced by the scattered light from brighter stars. For all the bands, we selected stars in this region using SExtractor with stellarity factor greater than 0.8 and a magnitude range between 15.5 and 16.5 mag. This magnitude range selects the brightest non-saturated stars. The number of selected stars for the stacking depends on the band, being around 600 stars.

We proceed as follows. We created a stamp of 201 pixels (≈ 80 arcsec) using SWarp centered at the coordinates retrieved from SExtractor of each star and we masked all the external sources. As in the case of very bright stars used for the construction of the Wing PSFs, having the most accurate measurement of the central coordinates of the stars is crucial to build a reliable Core PSF. We discarded the use of coordinates from catalogues. Instead, we fitted a Moffat function to each star using IMFIT (Erwin 2015) and we resampled the stamp using the coordinates retrieved by the Moffat best fit. We recalibrated the sky of each star at a radius larger than 80 pixels. To perform the normalization of each star, we measured the flux of the profile from 9 to 11 pixels (≈ 3.5 to 4.5 arcsec). Finally, we obtained the Core PSF by stacking all the stars using a resistant mean with a 2σ rejection.

Appendix B.3: Junction of the complete PSFs

To obtain the complete PSFs, we performed the junction of the Core with the Wing PSFs for each of the u , g , r , i and z bands. The main difficulty of this process is the normalization and the relative sky reference of the Core PSF in relation to the Wing PSF. By construction, the sky measured around the stars for creating the Core PSFs (region beyond 80 pixels) is calibrated over a region where there is flux of the Wing PSF, although underneath the noise. This implies having to perform a junction with 2 free parameters, as they should match in flux in the junction point but also they should have a common absolute sky reference, which is unreliable to obtain due to the low signal to noise of the Core PSF at large radius (where the sky reference has been calibrated for the Wing PSF). To solve this problem, we performed the junction of Core and Wings by solving the following set of equations.

$$\text{Core}(R1) = a \times \text{Wing}(R1) + b$$

$$\text{Core}(R2) = a \times \text{Wing}(R2) + b$$

Where R1 and R2 are two different radial distances with enough signal to noise in both the Wing and Core PSFs radial profiles. Hence, solving these equations will give us the normalization value (a) and sky level (b) to be applied to the Core PSF for a perfect matching previous to the junction. We use different R1 and R2 radial distances for each band trying to avoid the internal reflections and reaching the best signal to noise as possible for the final PSFs (see Infante-Sainz et al. 2019 in prep., for further details). After the normalization of the Core PSFs relative to the Wing PSF we performed the junction. Pixels less than R1

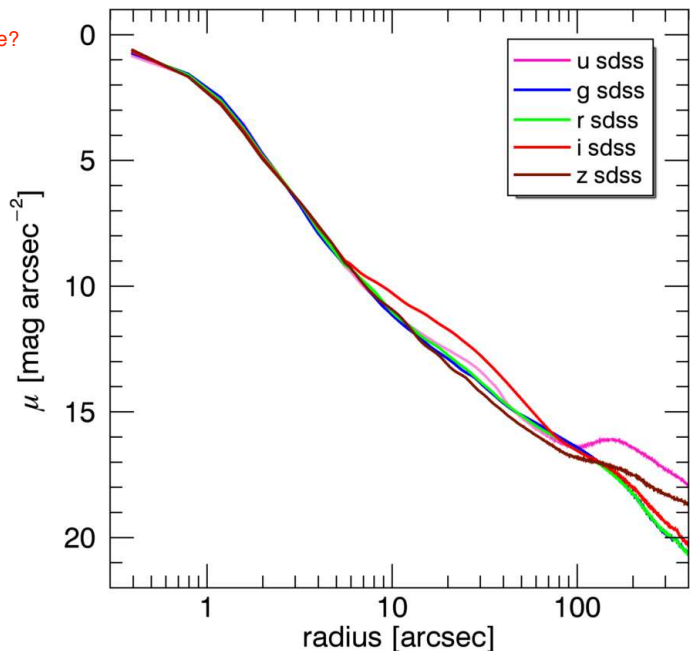


Fig. B.2. Radial profiles of the IAC Stripe82 PSFs obtained and used in this work.

away from the center are referenced to the Core PSF, and pixels with a larger radius are referenced to the Wing PSF, producing the complete PSF. We show the profiles for the complete PSFs of each band in Fig. B.2.

Appendix C: Estimation of photometric errors for the Galactic cirri diffuse emission.

In this Appendix we expand on the details of the methodology used to obtain the colors of the Galactic cirri. We also perform a set of simulations to quantify the uncertainties in this measurement.

Due to the Poisson nature of the noise in the images, the color distribution of that noise using two bands follows a Lorentzian distribution. As the definition of magnitude involves the use of logarithm, only positive values of flux have physical sense. Therefore, for a given pixel to enter in the color distribution, both bands A and B in that pixel must have a positive flux (for pixels with no source emission, only one in four pixels will enter in the distribution on average). Because in general, the depths of both bands are not the same (or widths of their Gaussian distributions), this causes the Lorentzian color distribution to off-center from zero. In other words, given a pixel, its most likely color will be dominated by the flux of the shallower band (higher Gaussian dispersion). For example, two photometric bands A and B with limiting depths of $\mu_A = 25.5$ and $\mu_B = 25.0$ mag arcsec $^{-2}$ will produce a Lorentzian distribution centered in the color $A-B = 0.5$ mag arcsec $^{-2}$.

In the left panel of Fig. C.1, we show the color distribution of pixels in the processed (see Sec 2) Control field (see Fig 6). Due to the absence of extended diffuse emission, the color distribution of the pixels in this field can be considered exclusively due to the noise of the image. We fit this distribution with a Lorentzian function. As can be seen, the fitting shows an excellent match with the observed color distribution. The centers of the fitted Lorentzian distributions are $x_L = 0.39, 0.52$ and 1.06 mag for the $g-r$, $r-i$ and $i-z$ colors respectively. While for the $g-r$ and $r-i$ colors the x_L values match the depth differences of those

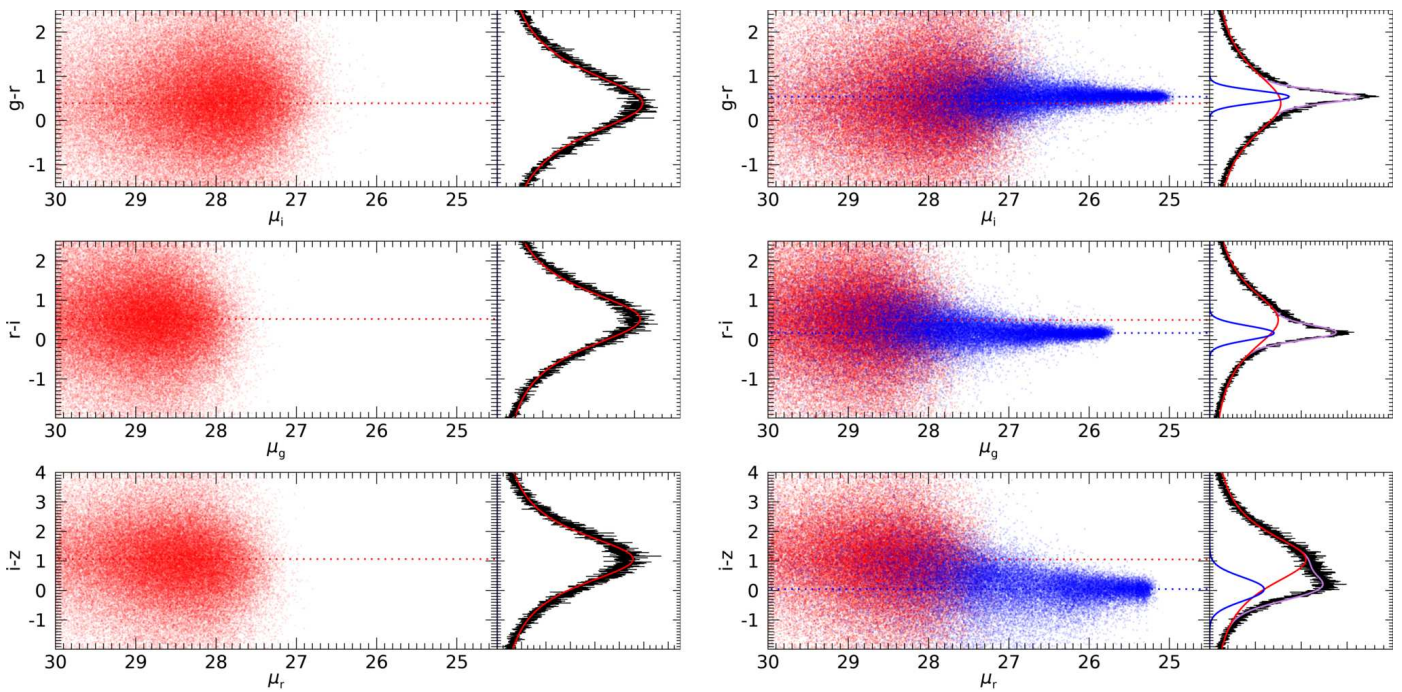


Fig. C.1. The color distribution of the noise in the Control Field and the resulting color distribution by adding an artificial constant color structure. Left panels: color vs. surface brightness values (red dots) of pixels dominated by the noise. Their color distribution is very well fitted by a Lorentzian function (red curve) as shown in the right side of the plot. Right panel: same but adding a constant color structure (blue dots) fitted by a Gaussian function (blue curve). The purple curve is the result of combining a Lorentzian plus a Gaussian function. The horizontal dashed lines correspond to the calculated centers of the Lorentzian and Gaussian functions.

bands, for $i-z$ this value differs by around 0.5 mag due to the higher sky fluctuations in the z band. Note also, that the depth values provided in Section A are average values of the entire survey. The depths of a particular field may vary with respect to the average values of the whole survey due to the specific observational conditions in that field.

The color of any source present in the field will be added to this Lorentzian color distribution of the noise. There will be a transition from the color of the noise to the color of the source as the signal or surface brightness of the source increases. For the fitting corresponding to the color of the source we use a Gaussian function. Therefore, we perform the fitting of the color distribution of a field with presence of dust with a Lorentzian plus a Gaussian functions, as described in the Section 4.

In order to quantify the uncertainties in the photometry of the Cirri, we perform a set of simulations injecting a structure of known color. This structure is used as a mock Galactic cirri, and the process for recovering its color is done by the described method. The injected structure has an area corresponding to approximately one fifth of the total area of the field and consists of a rectangle whose surface brightness decays on one axis, simulating the properties of the observed cirri, in which a wide range of surface brightness is found. The brightest region of this structure has a surface brightness of 25.5 mag arcsec $^{-2}$ and the faintest 30 mag arcsec $^{-2}$ in the g band, well below the detection limits of the data. We show in the right panel of Fig. C.1 an example of the inclusion of such structure in the Control field. This structure has colors of $g-r = 0.55$, $r-i = 0.15$ and $i-z = 0.05$. Using our method, we recovered the following colors $g-r = 0.537$, $r-i = 0.168$ and $i-z = 0.045$, showing the accuracy and reliability of the proposed method. Note that although the color of the structure is constant, the recovered distribution is not a Delta function

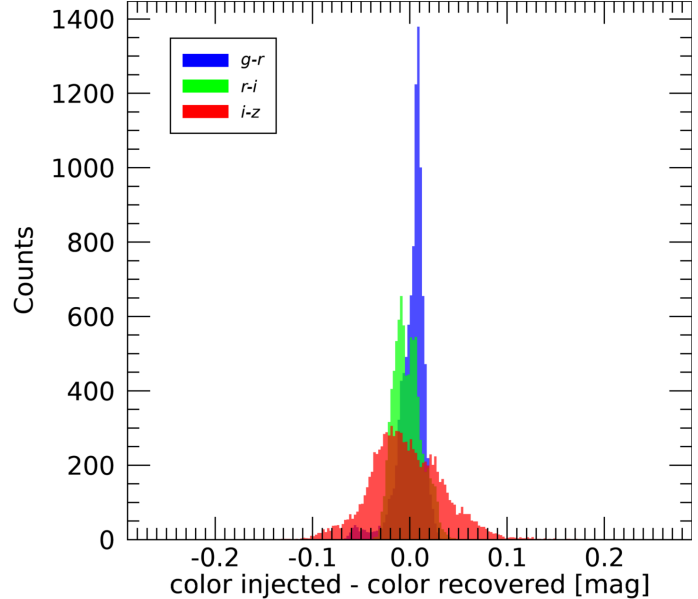


Fig. C.2. Differences between the injected and recovered colors of the mock Galactic cirri in the simulations.

but a Gaussian function due to photometric uncertainties and the underlying sky background fluctuations.

We performed a number of 10,000 injections / recoveries of such structures. In each iteration, we placed them in random positions within the field, avoiding a potential bias that could be introduced by locating the structures in the same area, for instance, anomalous sky fluctuation. The colors of the structures are also randomly drawn in each iteration, within the range [0,1] mag for $g-r$, and [-0.5,0.5] mag for $r-i$ and $i-z$. In Fig. C.2, we plot the his-

togram of the difference between the injected and recovered $g-r$, $r-i$ and $i-z$ colors. These colors follow an approximately Gaussian shape with slight deviations in their mean values with respect to 0 mag. The mean values of the distributions are -0.0066 mag, -0.0115 mag and -0.0085 mag for the $g-r$, $r-i$ and $i-z$ colors respectively, and therefore, negligible. The 3σ standard deviations of these distributions are: 0.04 mag, 0.04 mag and 0.11 mag for the $g-r$, $r-i$ and $i-z$ colors respectively. Therefore, we assume these values as the uncertainties for the measurement of cirri colors by this method.

Appendix D: Photometric maps of the Cirrus Field

In Fig. D.1 and Fig. D.2, we present the color maps of the Cirrus field discussed in Sec. 3.

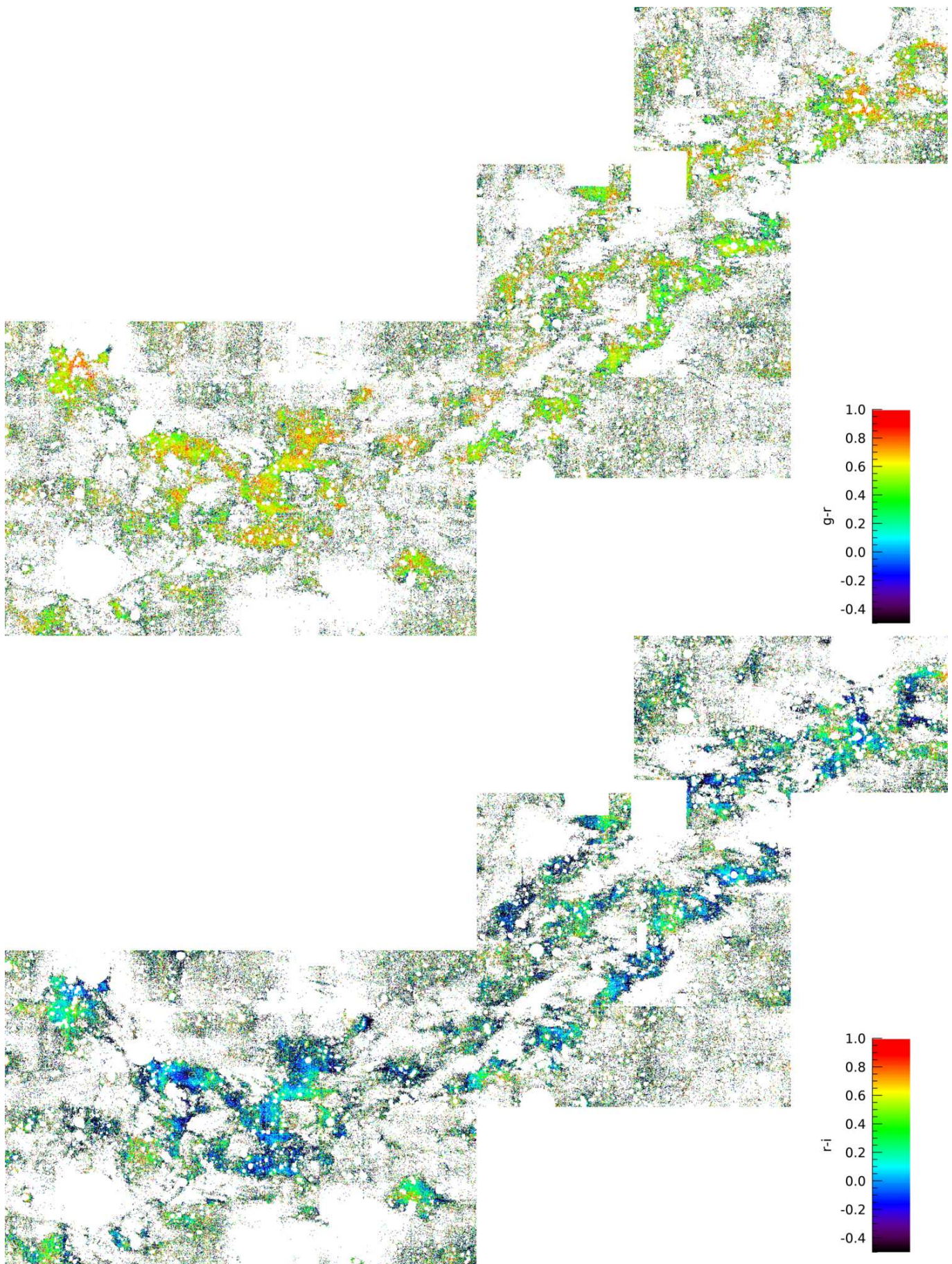


Fig. D.1. $g-r$ and $r-i$ color maps of the Cirrus Field.

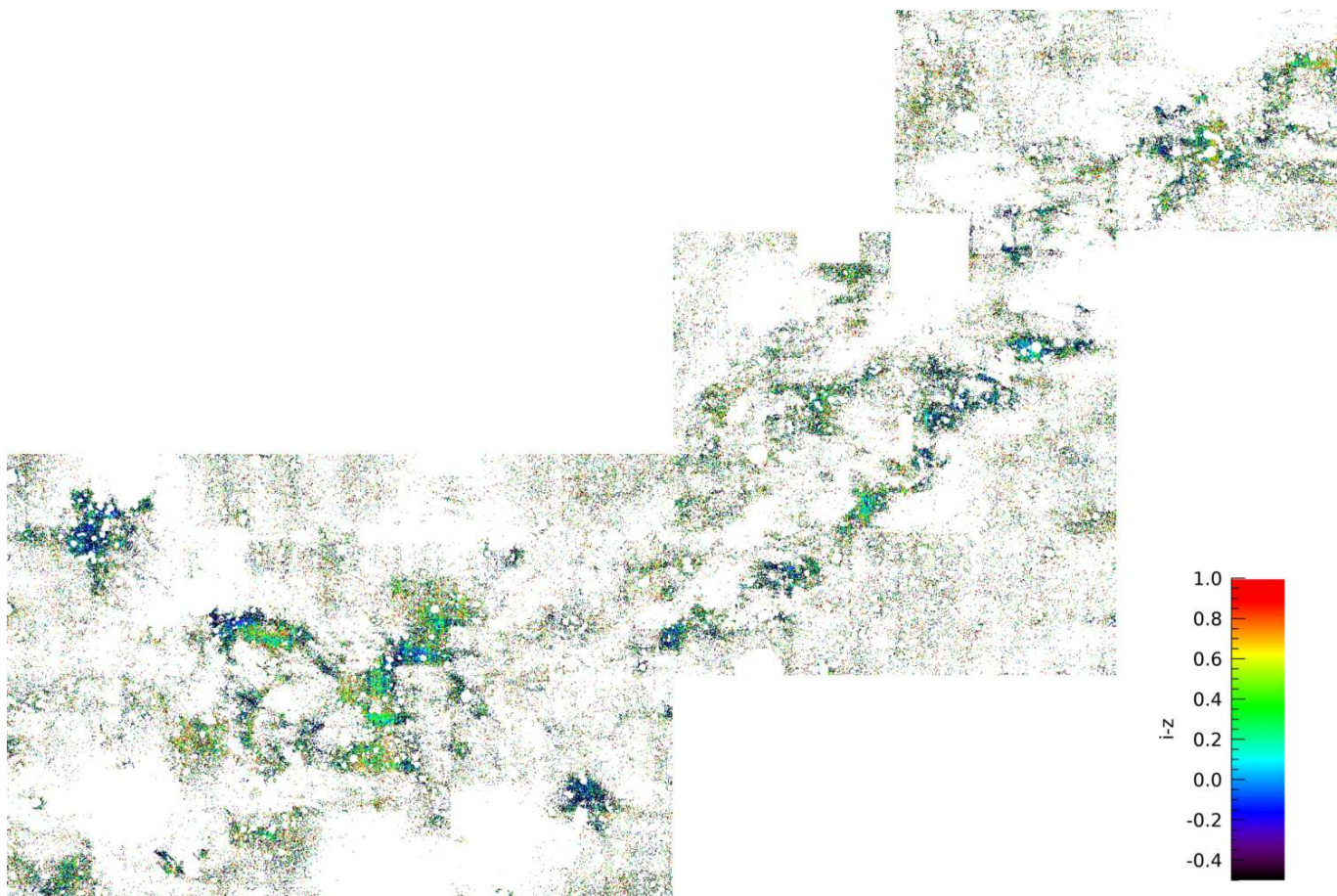


Fig. D.2. $i-z$ color map of the Cirrus Field.